united nations
educational, scientific
and cultural
organization

international atomic
energy agency

the
abdus salam
international centre for theoretical physics

SMR/1108 - 5

COURSE ON "MEDITERRANEAN SEA(S) CIRCULATION & ECOSYSTEM FUNCTIONING"
2 - 20 November 1998
Trieste, Italy

"Response and Multiscale Interaction"
(Transparencies)

S. BRENNER
Israel Oceanographic & Limnological Research Institute
Haifa, Israel

Please note: These are preliminary notes intended for internal distribution only.

Response and Multiscale Interaction

Range of response on various spatial and temporal scales

- Spatial
  - Basin scale thermohaline cell
  - Sub-basin scale gyres
  - Current systems
    - Algerian, AIS, MMJ
  - Mesoscale eddies
  - Submesoscale
    - convective chimney

} highly energetic and variable

- Temporal
  - Permanent
  - Recurrent
  - Transient
  - Long term trends and changes

Budgets

Heat

$$\frac{dQ}{dt} = A + Q_S - Q_R - Q_E - Q_H$$

long term $\rightarrow \frac{dQ}{dt} = 0 \Rightarrow$

$$-A = Q_S - Q_R - Q_E - Q_H$$

Observations indicate $A \simeq 7\ w/m^2$

$\Rightarrow$ must be corresponding heat loss through surface

Uncertainty of estimates shown in following table

Table 1. Estimation of the long-term average Mediterranean heat budget (in W m^{-2}).

	$\overline{Q_s}$	$\overline{Q_b}$	$\overline{Q_e}$	$\overline{Q_h}$	$\overline{Q_t}$	
Bunker et al. (1982)	202	52	101	13	36	
	202	68	101	13	20	
	202	68	130	11	−7	*
Garrett et al. (1993)	202	67	99	7	29	*
	166	67	99	7	−7	*
	202	67	133	9	−7	
Gilman and Garrett (1993)	186	77	99	7	3	**
Bethoux (1993)	195	69	120	13	−7	

* increased Q_E , Q_H

Forcing . heat flux - uncertainty

* Reduced Q_S by 18%

** Reduced Q_S & increased Q_R

Mass budget

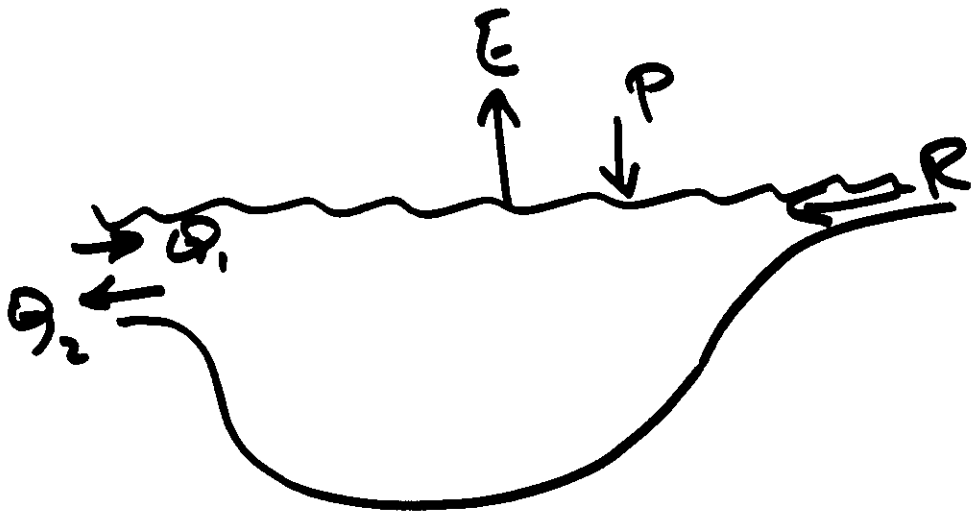

$$Q_1 + P + R = Q_2 + E$$

$$Q_1 - Q_2 = E - P - R$$

Must reconcile mass and heat budgets

$A \leftrightarrow Q_1, Q_2$

$E \leftrightarrow Q_1, Q_2$

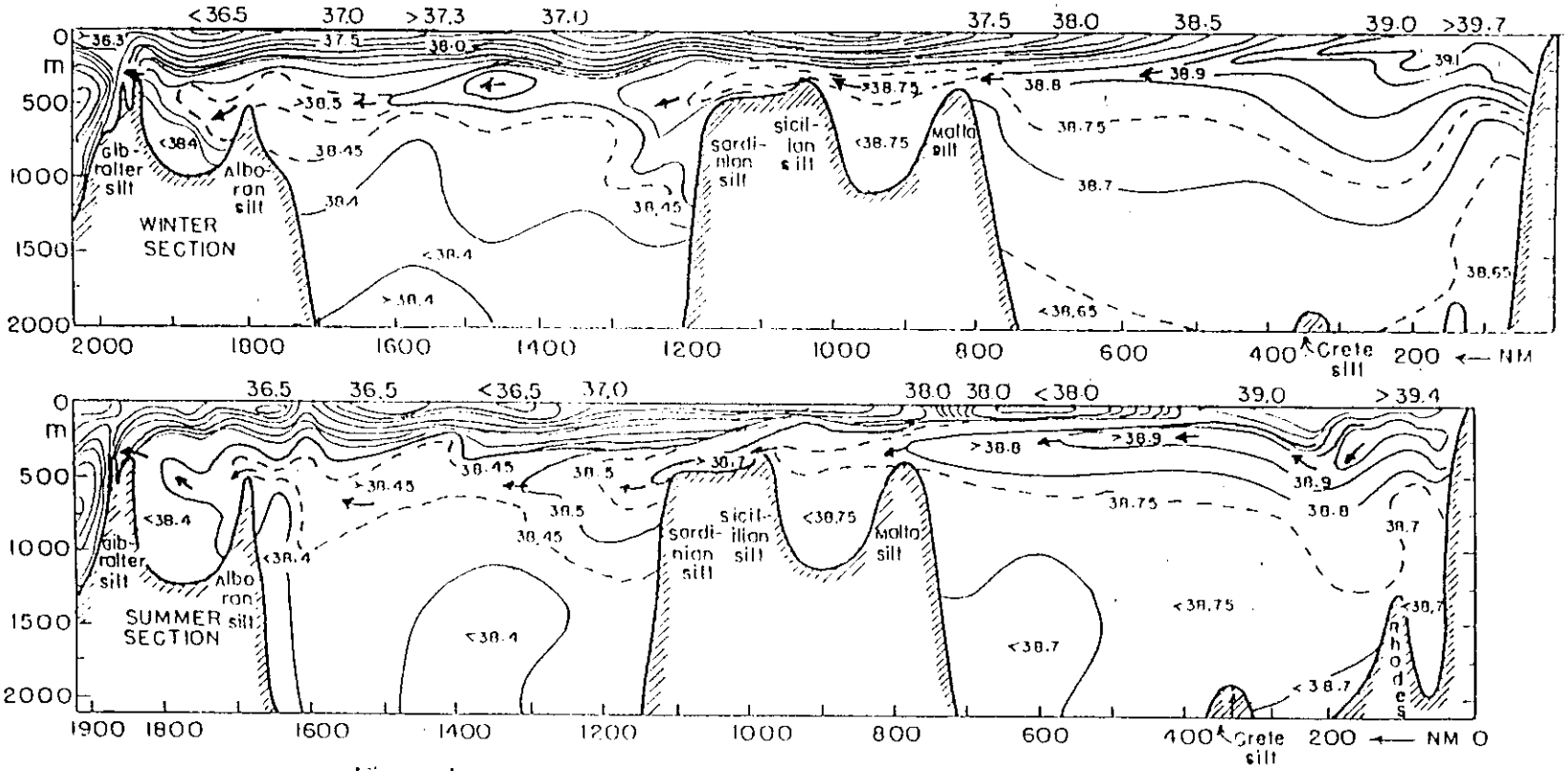

Figure 4

Core of the Levantine Intermediate Waters (LIW) along the Mediterranean Sea (from Wüst, 1961).

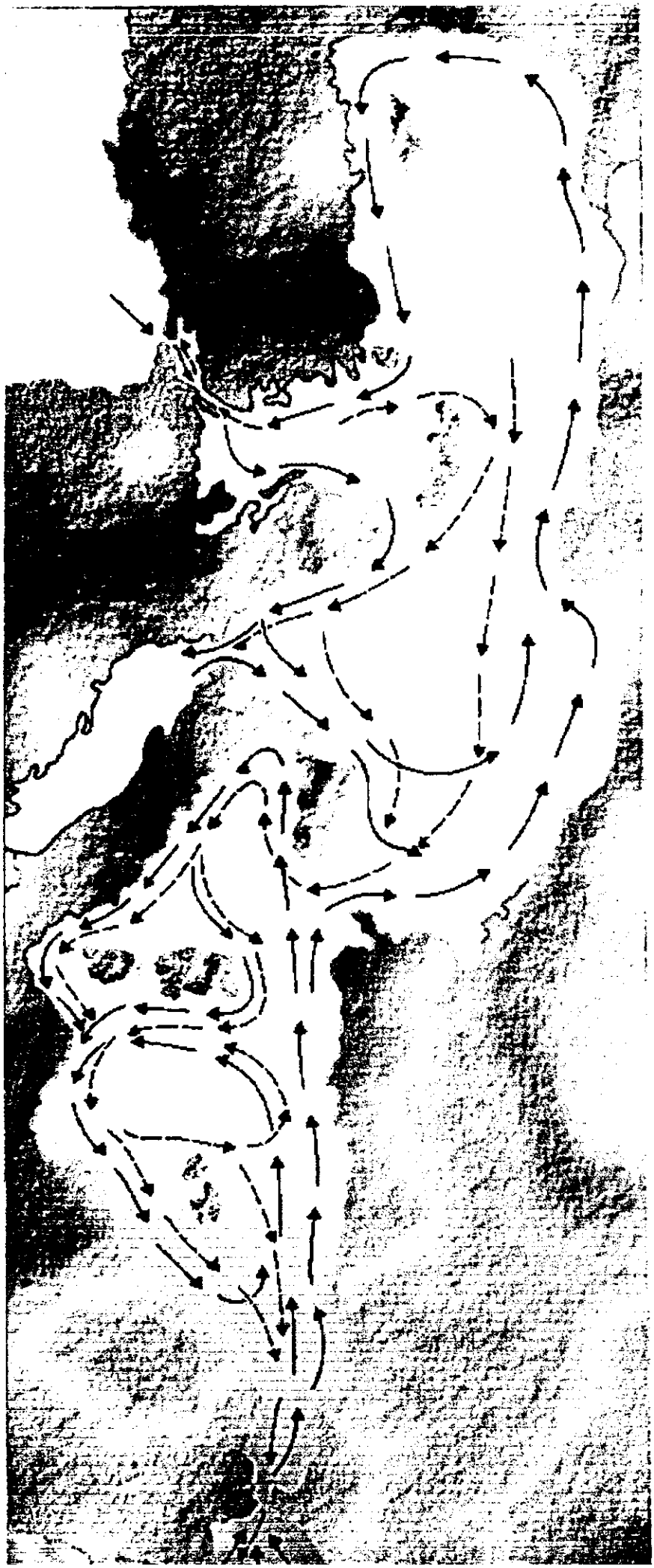

Nielsen (1912)

Water mass formation by convection

Three phases.

1. Preconditioning
2. Vigorous convection
3. Spreading

(a)

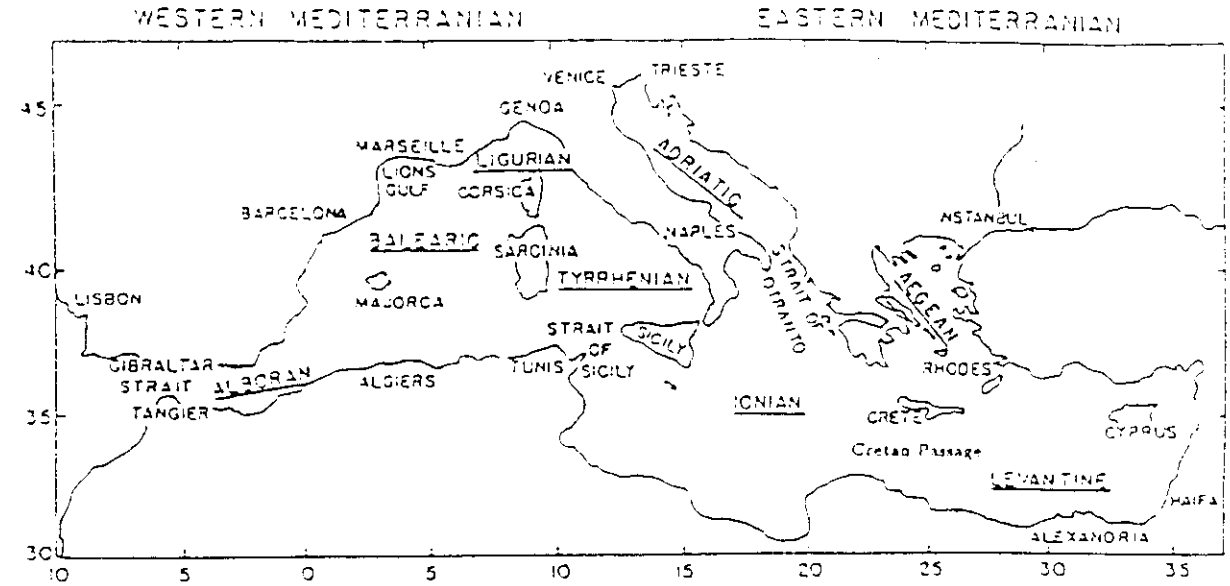

(b)

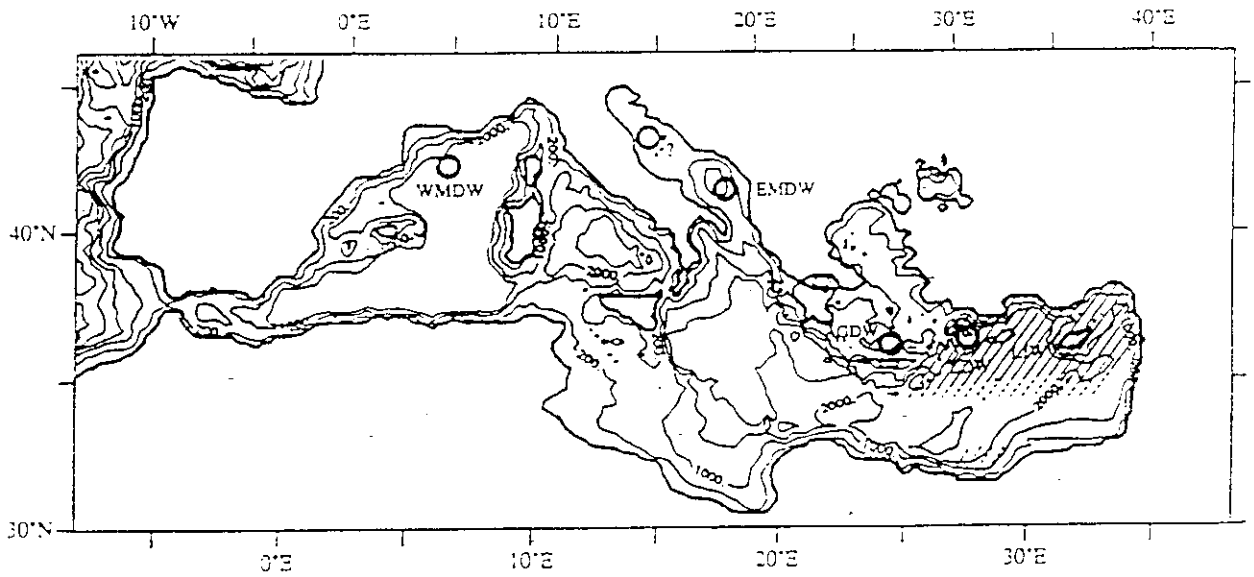

Figure 1: a) The Mediterranean Sea geography and nomenclature of the major sub-basins and straits. b) The bottom topography of the Mediterranean Sea (contour interval is 1000 m) and the locations of the different water mass formations.

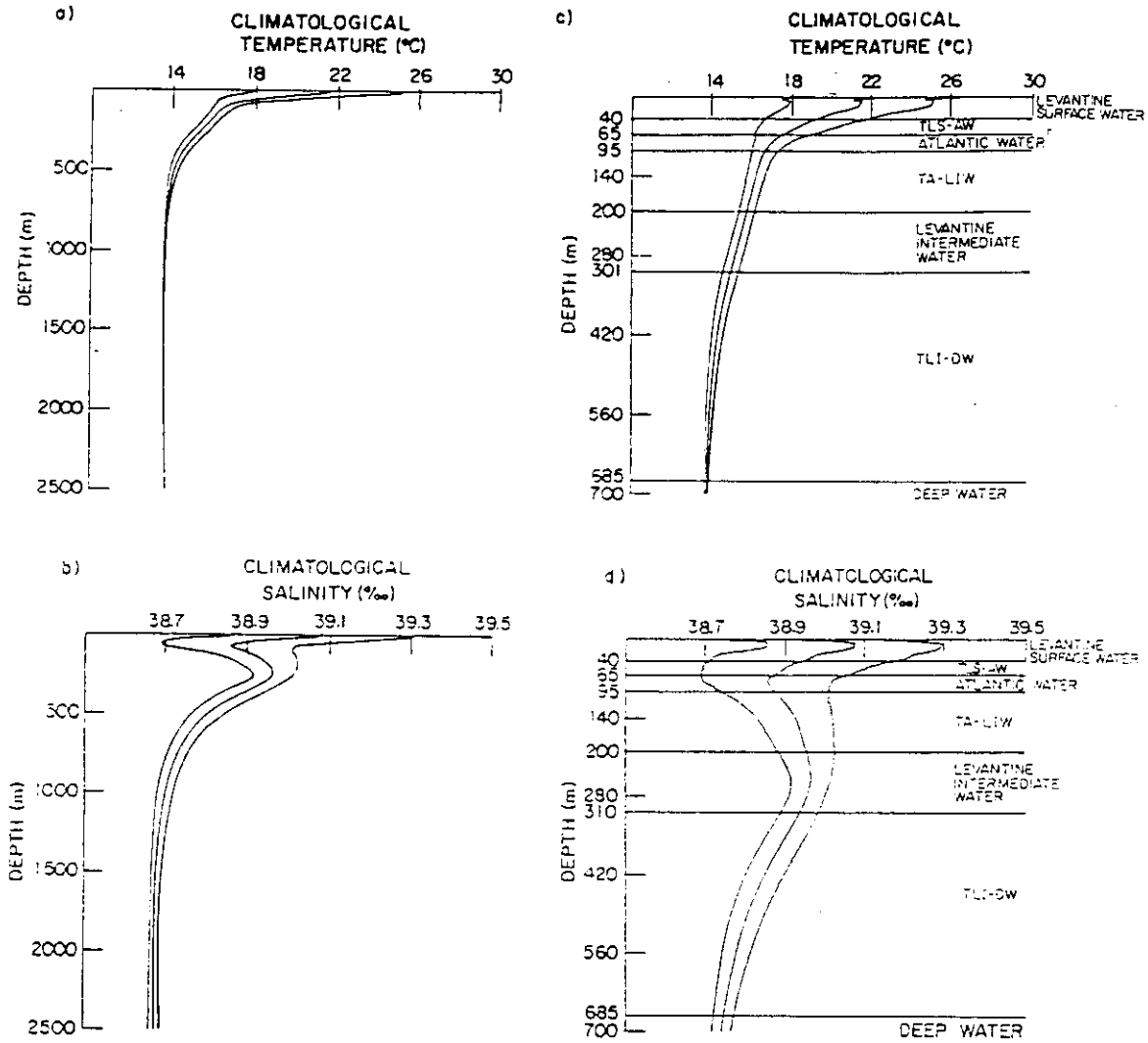

FIG. 4. (a) Climatological temperature profile as a function of depth (0–2500 m). (b) Climatological salinity profile as a function of depth (0–2500 m). The ±1 standard deviation profiles are also indicated. (c) As in (a) but for depth 0–700 m. The different layers characterizing the water masses of the region are indicated by horizontal lines. Abbreviations are explained in the text. (d) As in (c) but for the salinity profile.

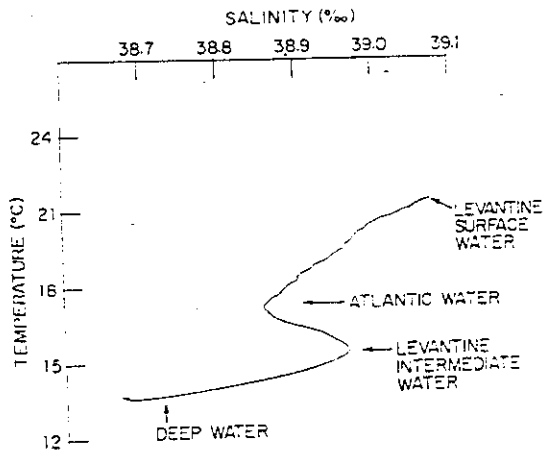

FIG. 5. Climatological T–S diagram showing the different water masses.

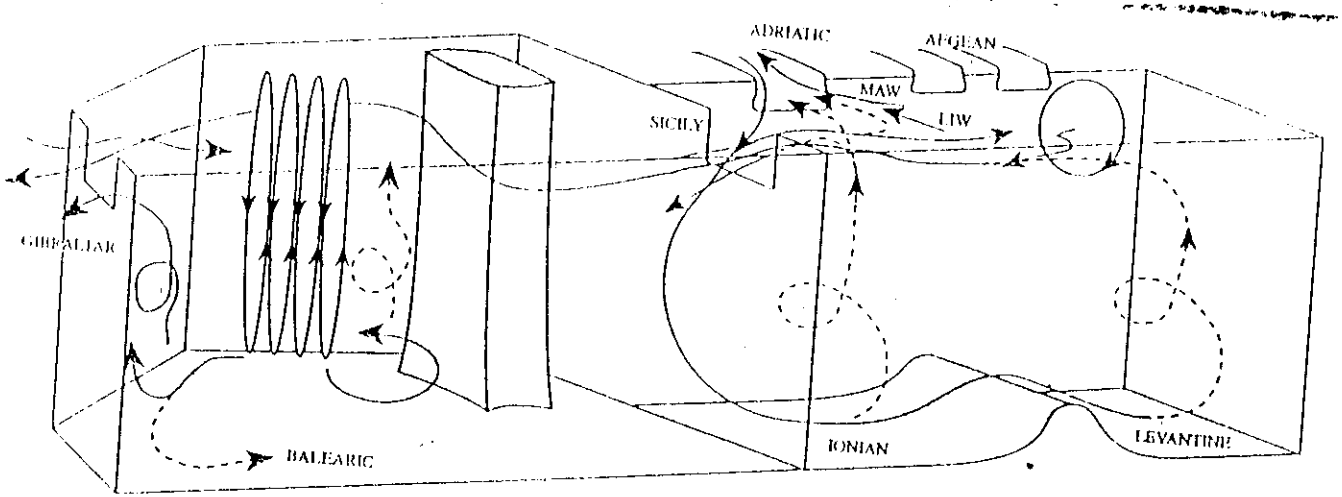

Figure 3: Schematic of thermohaline cells and path of LIW in the entire Mediterranean.

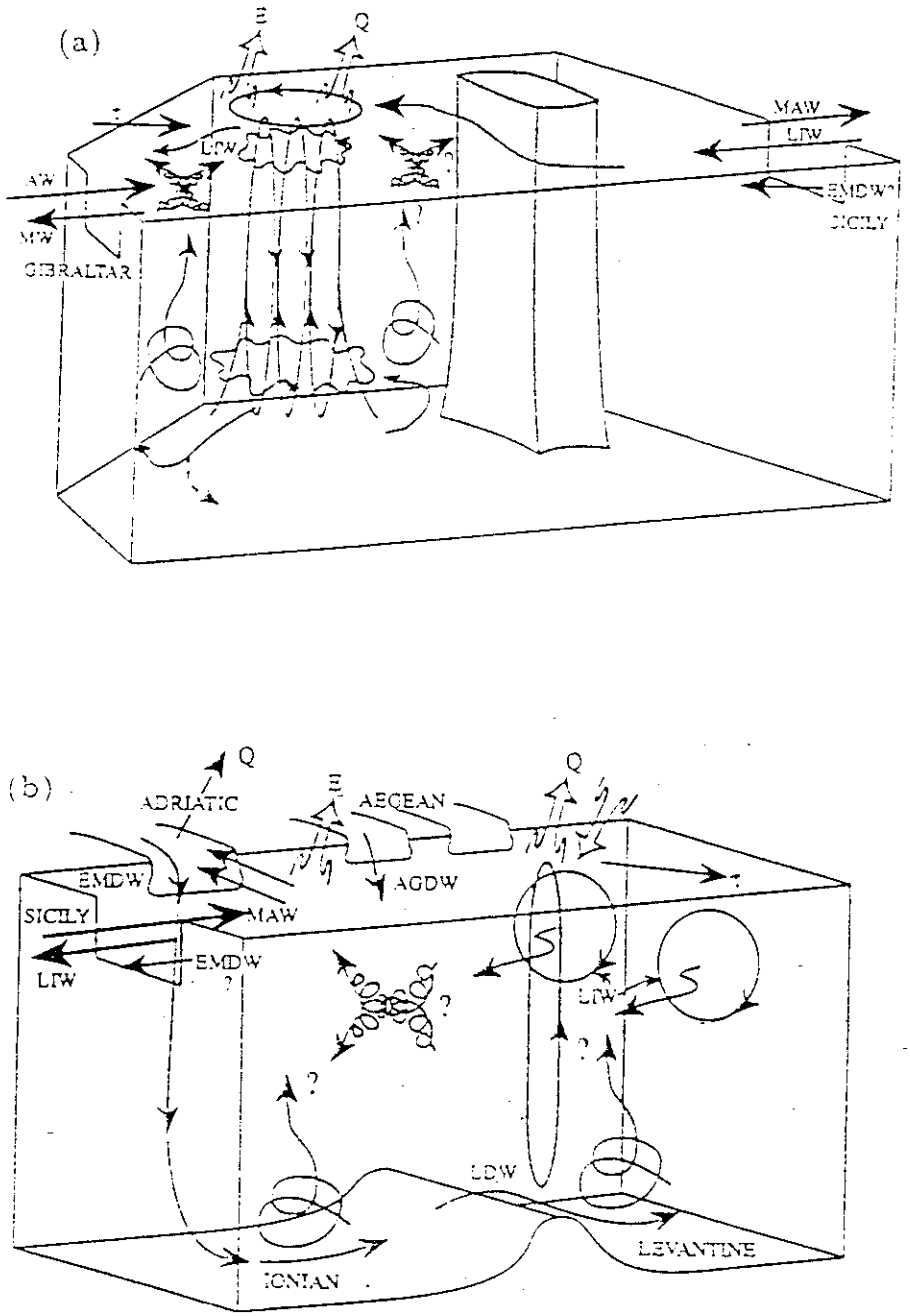

Figure 2: Processes of air-sea interaction, water mass formation, dispersion and transformation. a) Western Mediterranean. b) Eastern Mediterranean.

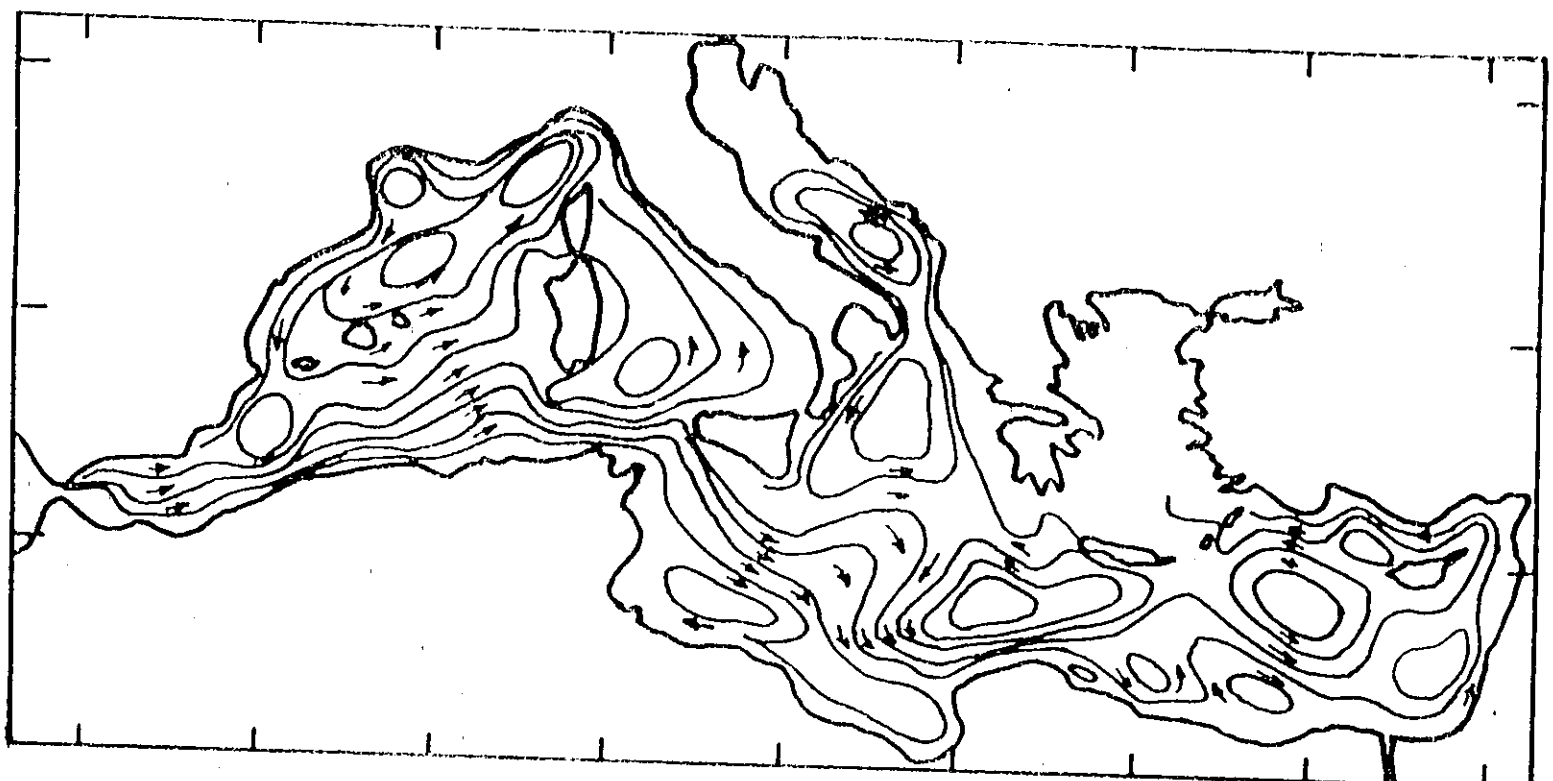

FIG. 2. Winter surface currents from dynamic height relative to 1000 m (reproduced from Ovchinnikov 1966).

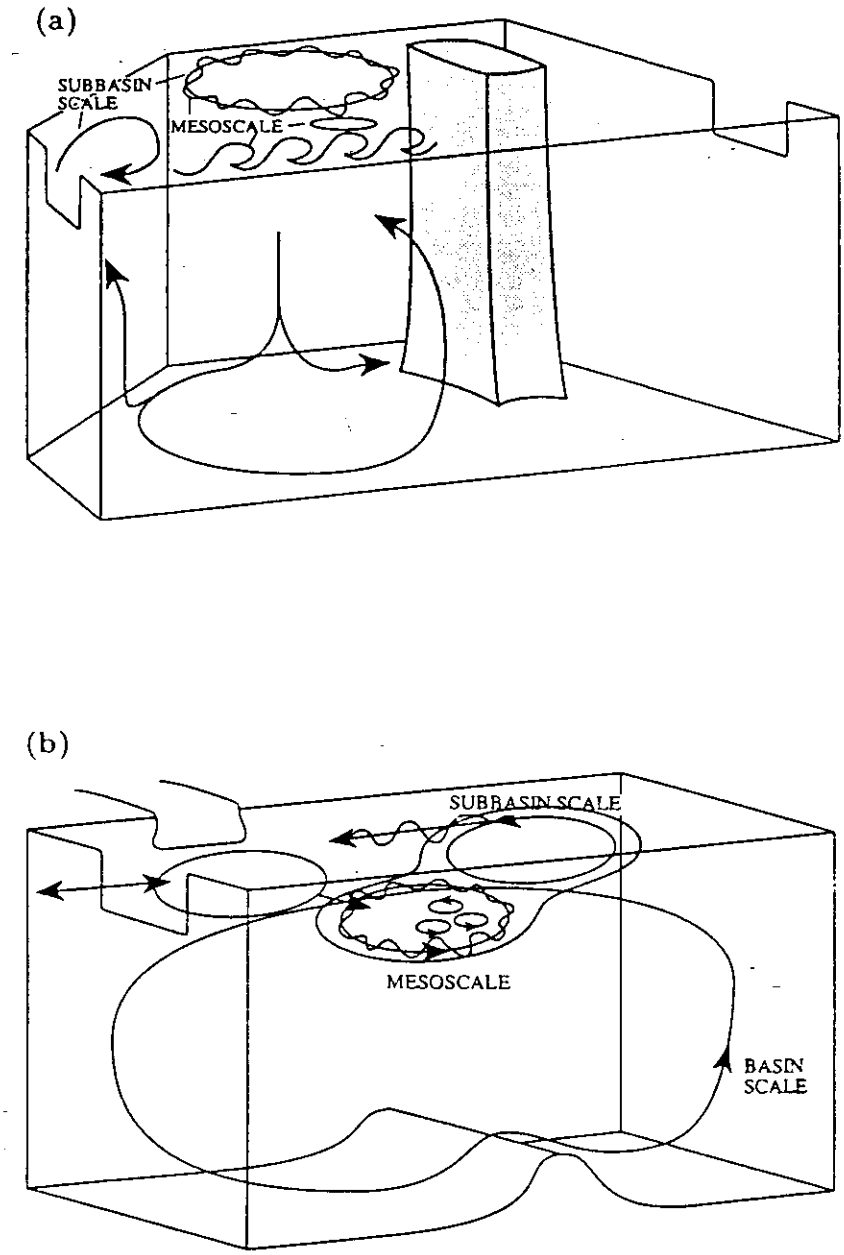

Figure 12: Schematic of the scales of circulation variabilities and interactions in, a) Western Mediterranean, b) Eastern Mediterranean.

Response - spatial scales

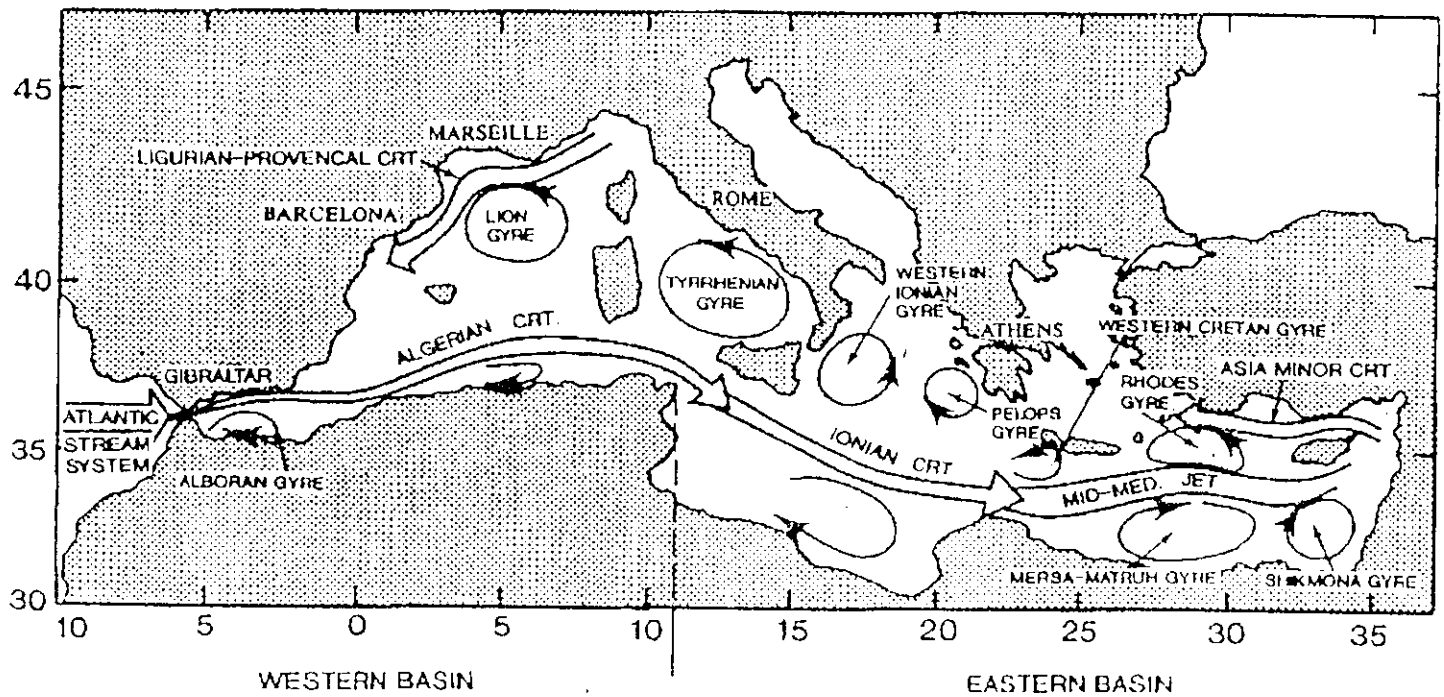
45
40
35
30
10
5
0
5
10
15
20
25
30
35
MARSEILLE
LIGURIAN-PROVENCAL CRT.
BARCELONA
LION GYRE
ROME
TYRRHENIAN GYRE
WESTERN IONIAN GYRE
ATHENS
WESTERN CRETAN GYRE
ASIA MINOR CRT.
RHODES GYRE
ALGERIAN CRT.
GIBRALTAR
ATLANTIC STREAM SYSTEM
ALBORAN GYRE
PELOPS GYRE
IONIAN CRT.
MID-MED. JET
MERSA-MATRUH GYRE
SI KMONA GYRE
WESTERN BASIN
EASTERN BASIN

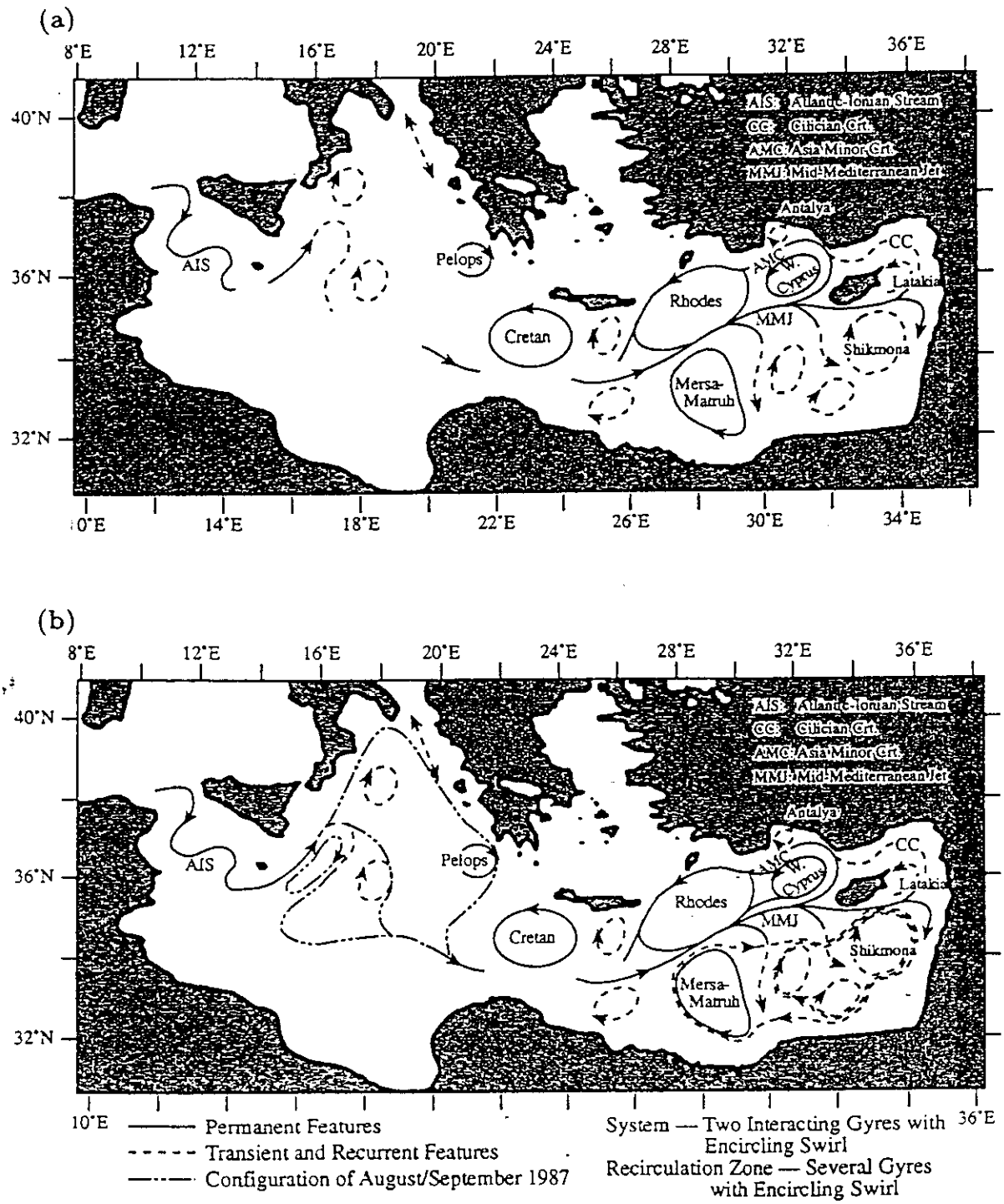

Fig. 2. (a) Schematic upper thermocline general circulation. Dashed features are recurrent or transient (ROBINSON *et al.*, 1991). (b) Schematic upper thermocline general circulation extended from melding of data and dynamics.

Response. spatial

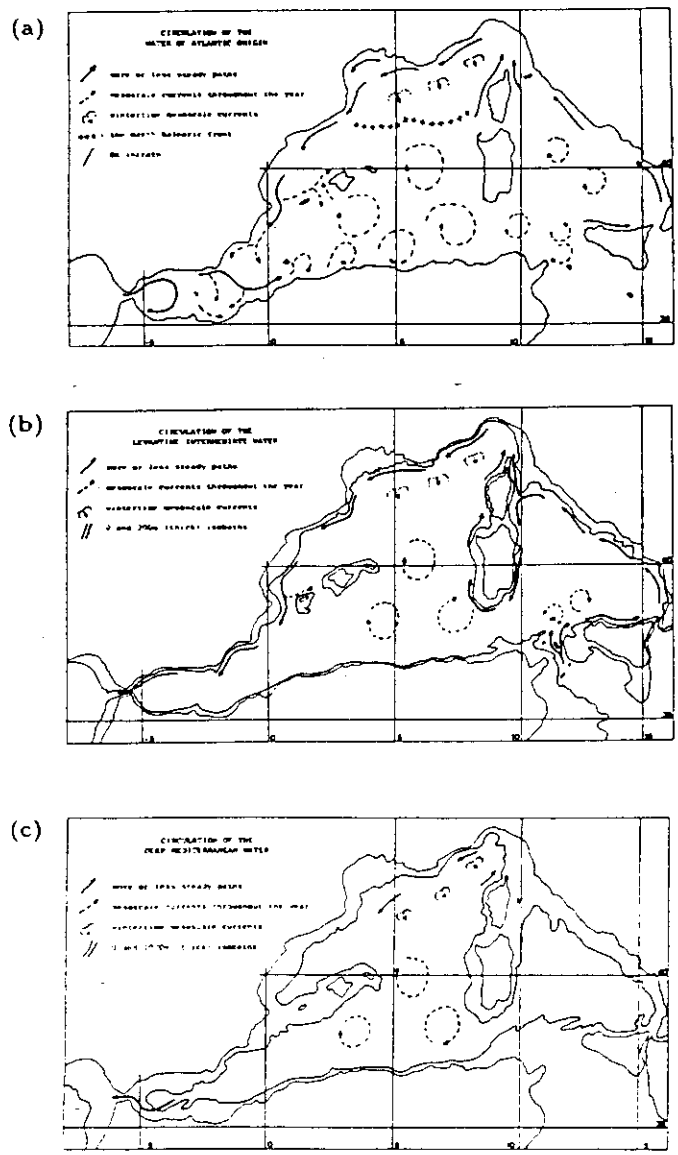

Figure 28: Schematic of the circulation in the Western Mediterranean. a) AW, b) LIW, c) DMW (Millot 1987).

response - spatial

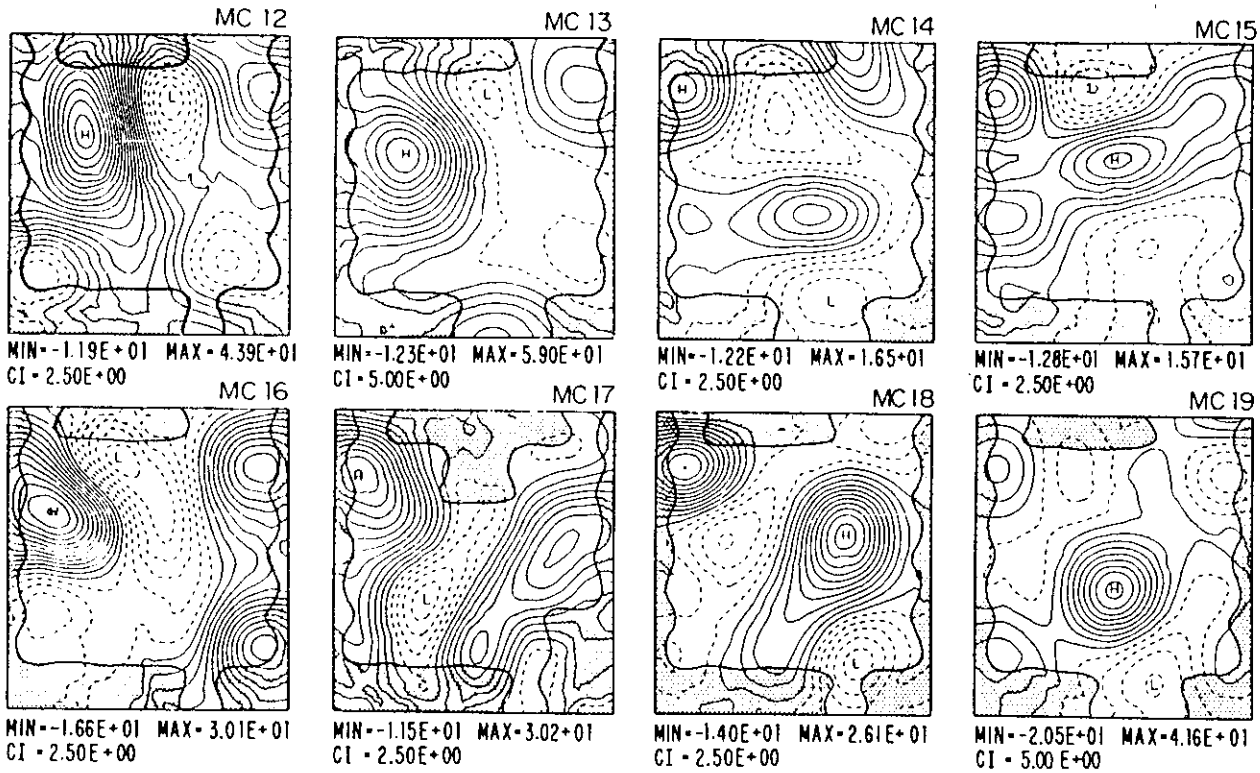

FIG. 16. The ϕ^* field at level 5 (230 m) for each cruise; the cruise number is indicated above each map. The values are nondimensionalized by $f_0 L_0$ (see text). The shaded areas indicate error variance greater than 40%. The min, max and CI below frames indicate the minimum, maximum and contour interval values.

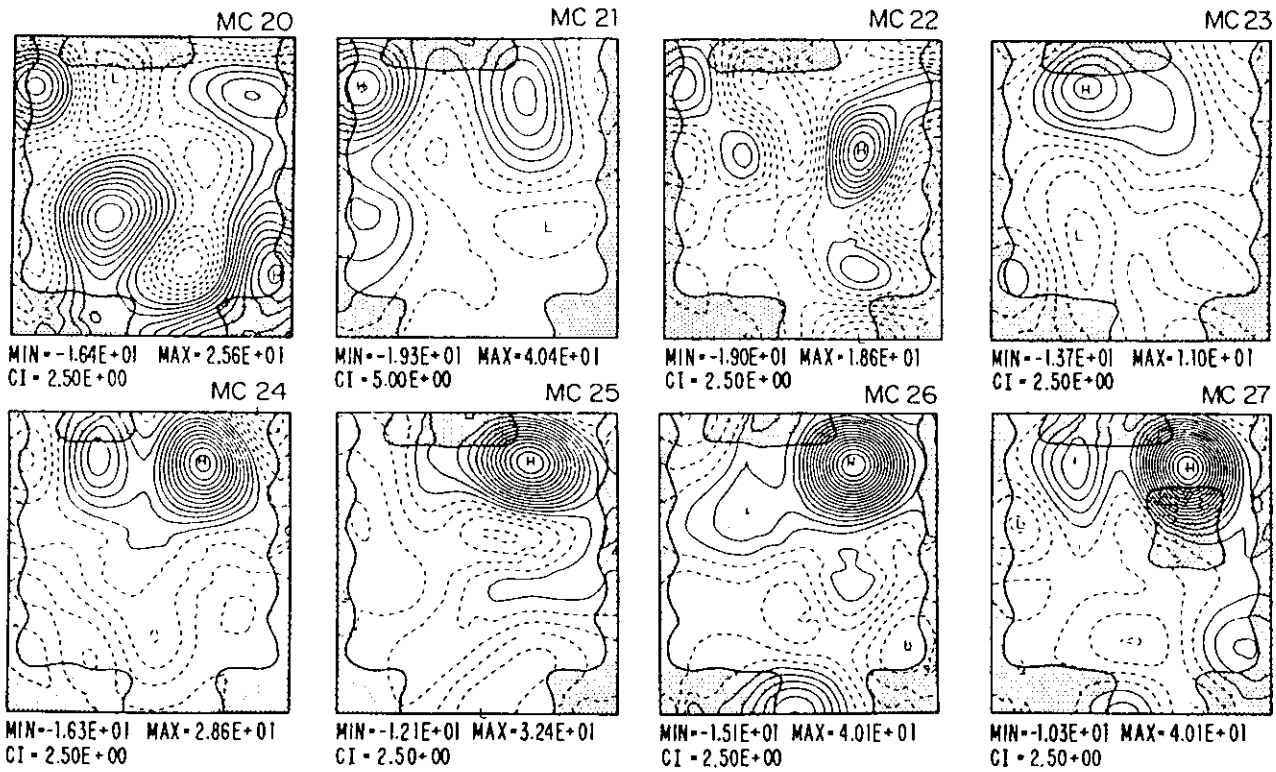

FIG. 16. (*Continued*)

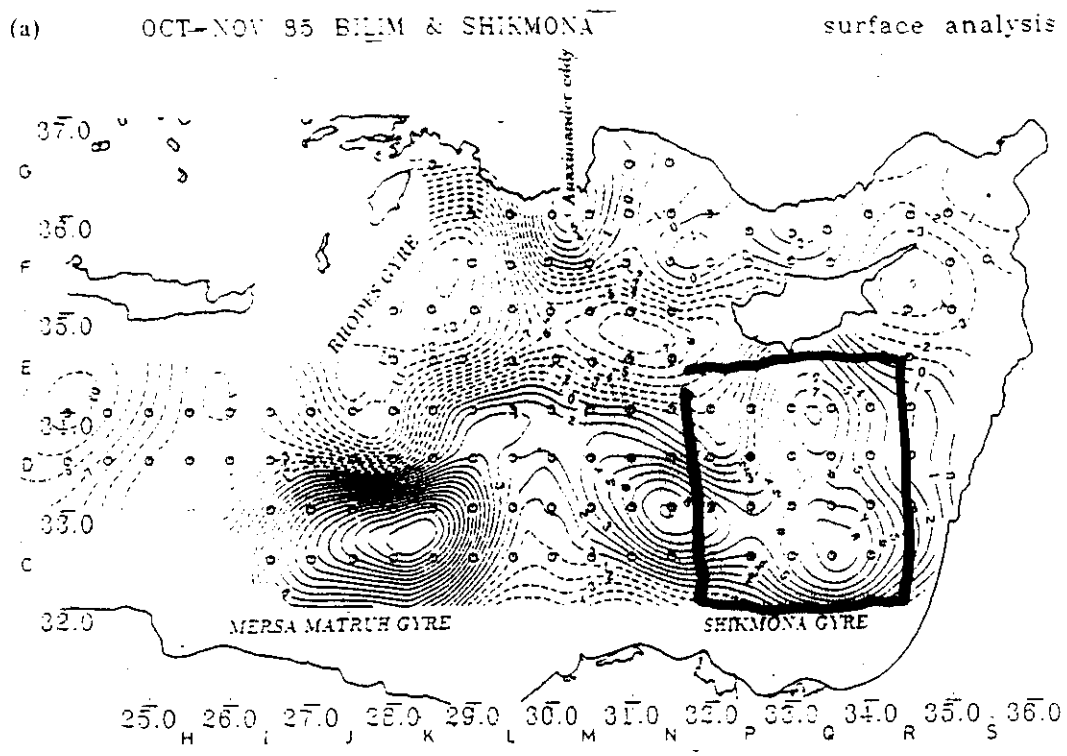

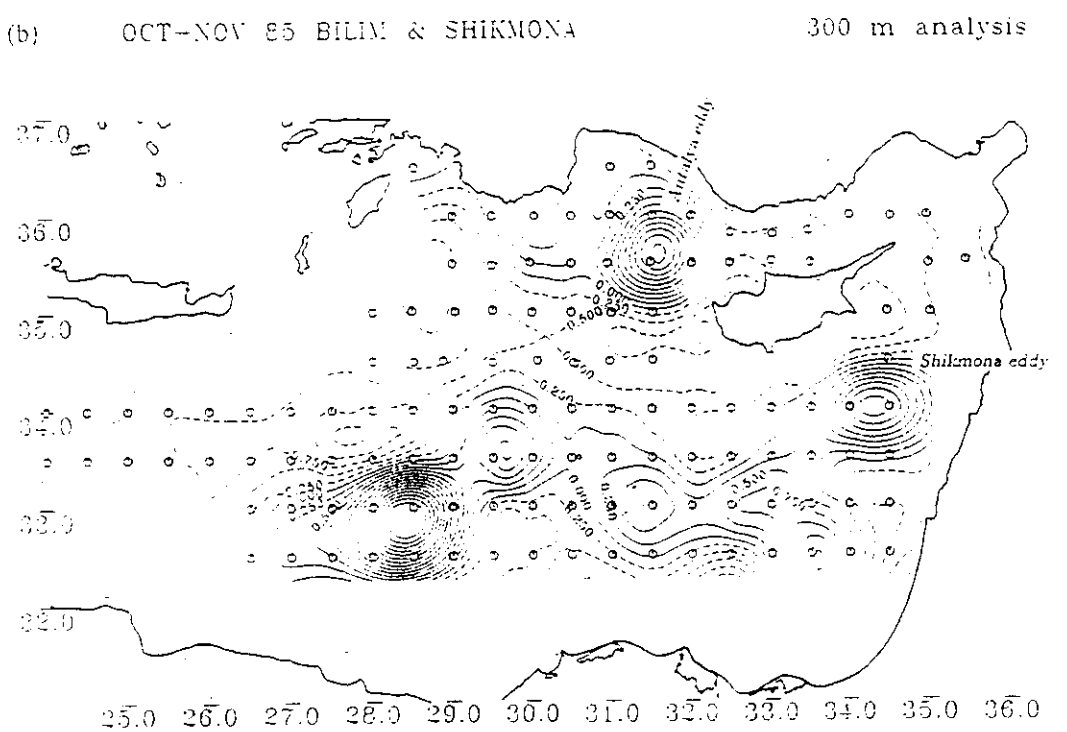

Fig. 2. (a) Surface and (b) 300 db dynamic height (in cm) referenced to 800 decibar level of no motion, October–November 1985. The one degree square letter coding used in station naming convention is also shown along the latitude and longitude divisions.

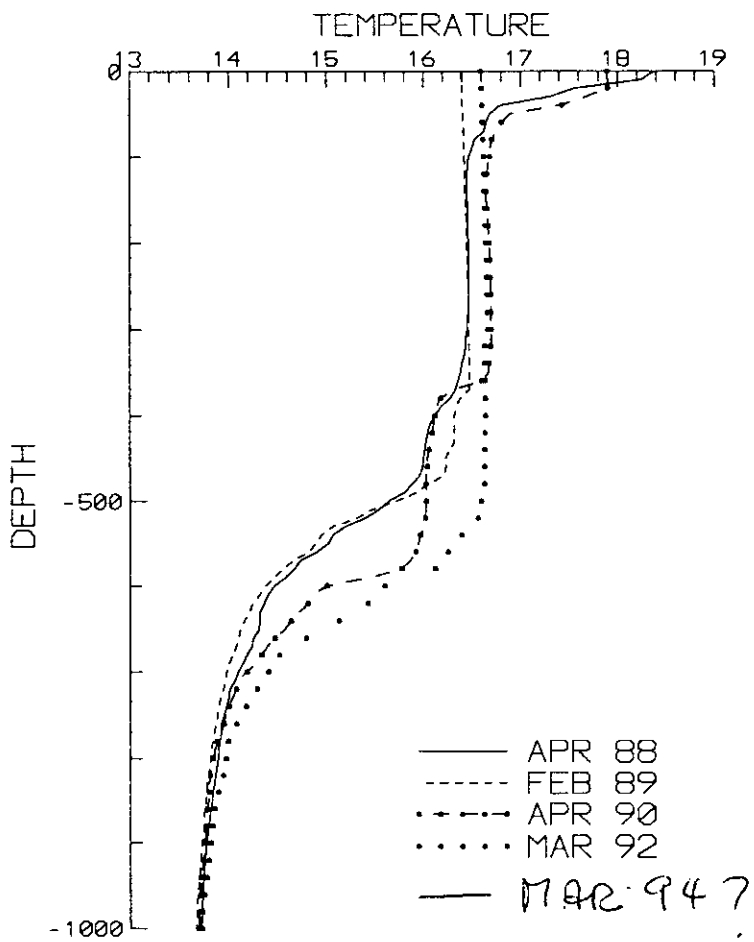

Subsequent cruises to Shikoku Gyre in Mar 92 (Severe winter, unusually deep mixing)

March 94 (Poseidon) - no eddy

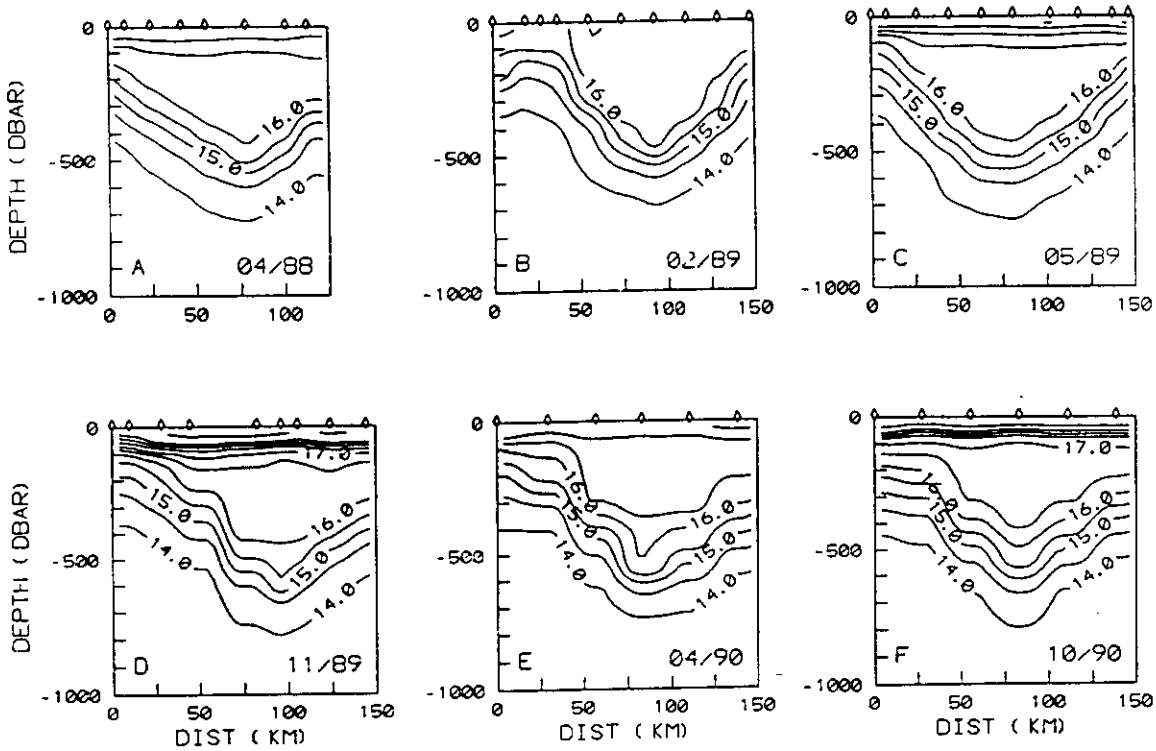

Fig. 3. North–south cross-section (north to the left) of temperature through the eddy: (a) April 1988; (b) February 1989; (c) May 1989; (d) November 1989; (e) April 1990 and (f) October 1990. Contour interval is 0.5°C up to 17°C, followed by 1°C up to 20°C, and 2°C above 20°C. Station positions are indicated along the top border.

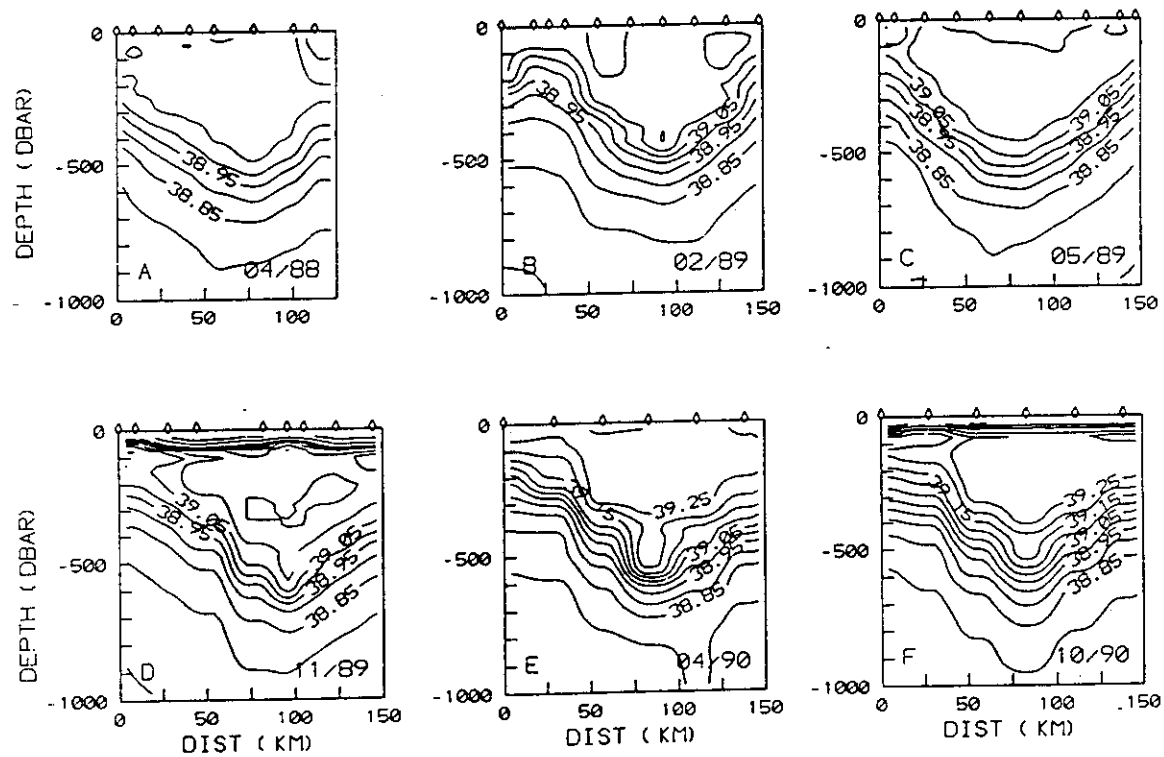

Fig. 4. As in Fig. 3, except for salinity. Contour interval is 0.05 up to 39.3 and 0.1 above 39.3.

Shikmona Thermostad Properties

Date	T	S	D	σ_θ
4/88	16.45	39.08	110-350	28.78-.82
2/89	16.44	39.15	0-370	28.84-.87
5/89	16.43	39.15	120-330	28.85-.87
9/89	16.43	39.15	130-380	28.85-.87
4/90	16.68	39.27	90-350	28.88-.89
10/90	16.68	39.27	120-400	28.88-.90
2/92	16.64	39.33	0-510	28.94-.96
2/94	—	—	—	—

Response. Long term changes / trends
in Deep water source.
multi equilib?

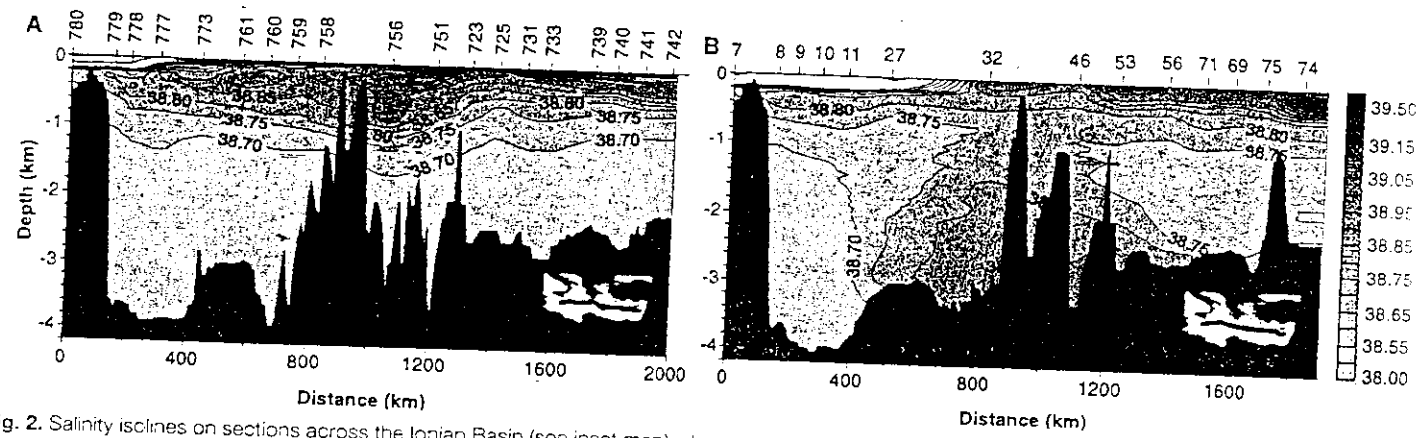

Fig. 2. Salinity isolines on sections across the Ionian Basin (see inset map); shown are data for *Meteor* cruises M5/6 (1987) (A) and M31/1 (1995) (B). Stations are at the top.

Fig. 3. Isolines of CFC-12 (pmol kg^{-1}) along the sections shown in Fig. 2. Shown here are data from cruises M5/6 (1987) (A) (no data beyond 1250 km) and M31/1 (1995) (B). Stations are at the top.

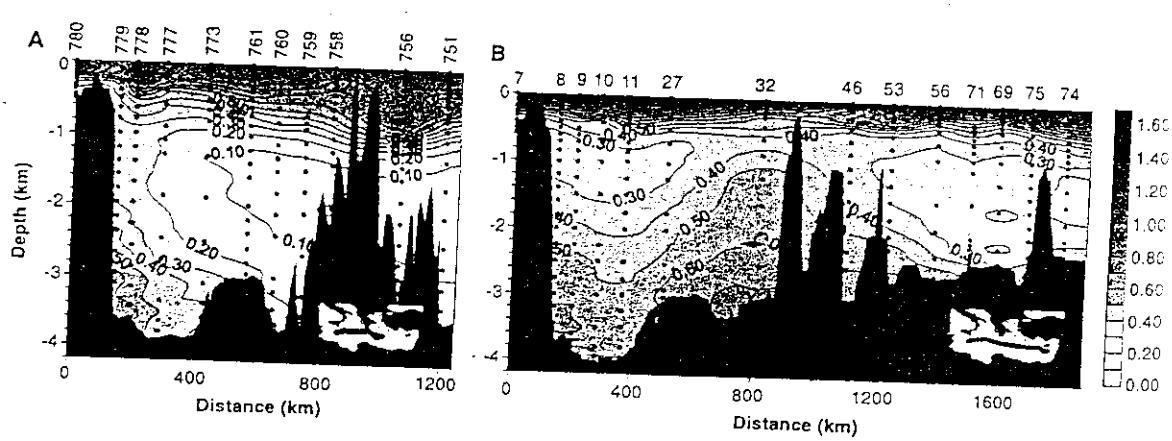

Fig. 4. Selected temperature-salinity diagrams for cruises M5/6 (1987) and M31/1 (1995), with density isolines (29 and 29.5 kg m^{-3}) superimposed; depth of 1200 m is indicated by open circles and the bottom by crosses; asterisks are 1995 *T-S* values at the sills of the Cretan Arc. (A) Stations 777 (M5/6) and 10 (M31/1), western Ionian Sea. (B) Stations 730 (M5/6) and 57 (M31/1), Levantine Basin. (C) Stations 759 (M5/6) and 37 (M31/1), eastern Ionian Sea. (D) Stations 753 (M5/6) and 41 (M31/1), Aegean Sea.

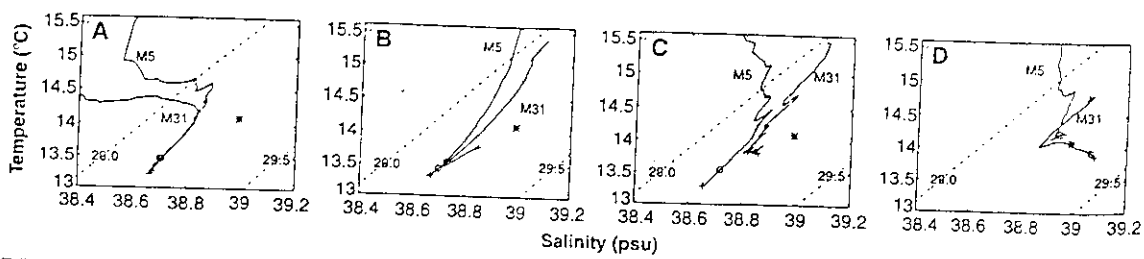

42

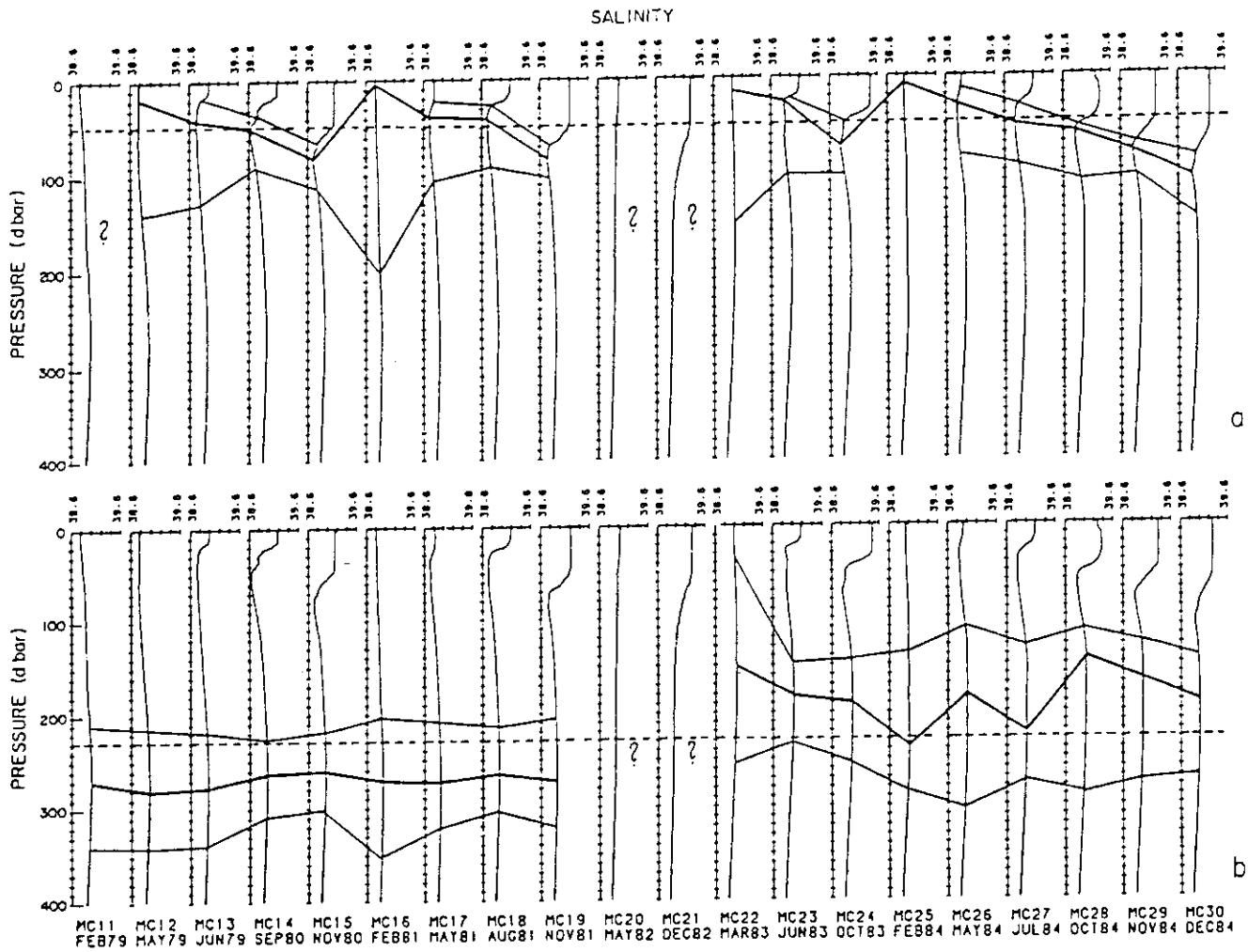

Figure 11

Depth and width of the AW (a) and LIW (b) layers on the sequentially organized salinity profiles from the MC cruises. The thick line indicates the cruise average depth of the layer, the two thin lines indicate the ± one standard deviation from the cruise average. The broken lines indicate the average depth of the layer.

Response long term trends

Note change in depth of LIW after 1982

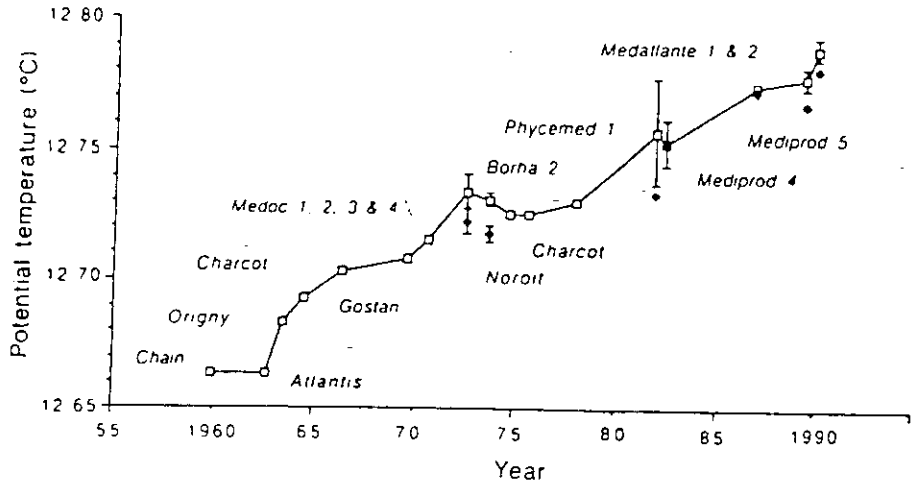

Figure 13: Potential temperature for the bottom water deeper than 2000 m in the Western Mediterranean (Bethoux *et al.*, 1990).

Response- Long term trends

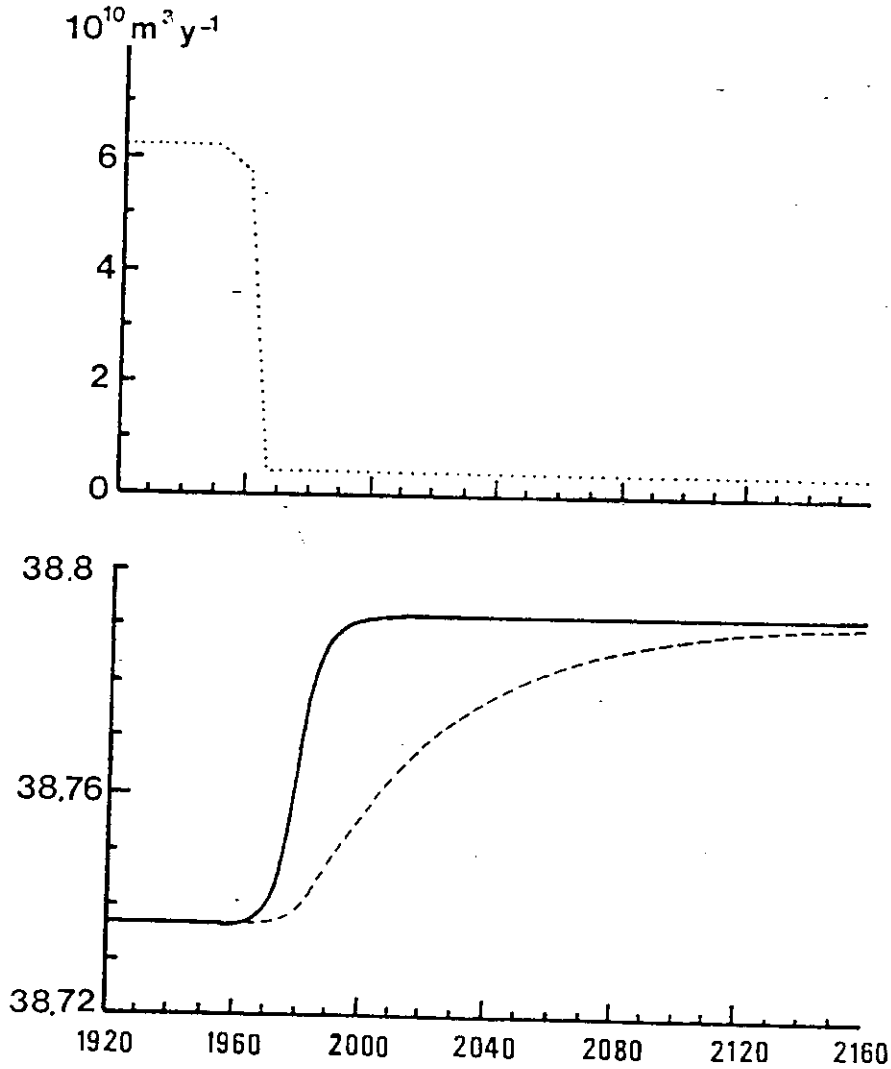

Figure 4. Upper part: evolution of the Nile river discharge over the period 1920-1973, marked by the closing of Aswan High Dam in 1964. Lower part: calculated evolution of salinities in the surface (continuoys line) and deep (broken line) waters of the eastern basin consecutively to the decrease of Nile river discharge since year 1960.

Forcing - fresh water input

Some basics of numerical modelling

Mathematical model - represent the behavior of the ocean and/or atmosphere through a set of equations derived from physical considerations

In other words —
The oceanographer's or meteorologists laboratory

Type or complexity depends upon:
- Process (es) to be studied
- Available data for initialization and validation
- Available computer resources

Model generally consists of a set of p.d.e. which in most cases can only be solved by numerical methods → Thus the numerical model

pde's usually approximated by a set of algebraic equations

Simplified vs. Complex model

Simplified- reduce complexity of full set of equations by various approximations or assumptions

advantages - fast, easy to solve
good for isolating processes

disadvantage- limited applicability

Complex. based on full or nearly full set of equations

advantage - simulates wide range of processes

disadvantage- simulates wide range of processes
expensive to run

Generic 3D hydrodynamic model (primitive equations)

$$\frac{\partial \underset{\sim}{v}}{\partial t} + \underset{\sim}{v}\cdot\nabla\underset{\sim}{v} + w\frac{\partial \underset{\sim}{v}}{\partial z} + f\,\underset{\sim}{k}\times\underset{\sim}{v} = -\frac{1}{\rho_0}\nabla p + A_H\nabla^2\underset{\sim}{v} + \frac{\partial}{\partial z}\left(A_V\frac{\partial \underset{\sim}{v}}{\partial z}\right) \quad (1)$$

$$\frac{\partial p}{\partial z} = -\rho g \quad (2)$$

$$\nabla\cdot\underset{\sim}{v} + \frac{\partial w}{\partial z} = 0 \quad (3)$$

$$\frac{\partial T}{\partial t} + \underset{\sim}{v}\cdot\nabla T + w\frac{\partial T}{\partial z} = K_H\nabla^2 T + \frac{\partial}{\partial z}\left(K_V\frac{\partial T}{\partial z}\right) + \frac{\partial R}{\partial z} \quad (4)$$

$$\frac{\partial S}{\partial t} + \underset{\sim}{v}\cdot\nabla S + w\frac{\partial S}{\partial z} = K_H\nabla^2 S + \frac{\partial}{\partial z}\left(K_V\frac{\partial S}{\partial z}\right) \quad (5)$$

$$\rho = \rho(T, S, p) \quad (6)$$

$\underset{\sim}{V} = (u, v)$ - horizontal velocity

w - vertical velocity

f - Coriolis parameter $(2\Omega \sin\phi)$

p - pressure

ρ - density

g - gravity

T - temperature or potential temp

S - salinity

R - penetrative shortwave radiation

A_H, A_V, K_H, K_V - "diffusion" coefficients

(1) Momentum equations ($F = ma$)

(2) Hydrostatic equation
vertical momentum equation for small aspect ratio

(3) Conservation of mass
incompressible fluid

(4) Conservation of heat

(5) Conservation of salinity

(6) Equation of state

Following (4) and (5) we can write a conservation law for any other substance, F

$$\frac{\partial F}{\partial t} + \underset{\sim}{v} \cdot \nabla F + w \frac{\partial F}{\partial z} = \underline{K_H \nabla^2 F} + \underline{\frac{\partial}{\partial z}\left(K_v \frac{\partial F}{\partial z}\right)} + \underline{X}$$

X = sources and/or sinks of F
(e.g. biological activity)

Underlined terms are the subgrid scales processes that must be parameterized - i.e., model cannot explicity resolve them

Vertical component of subgrid scale processes is often referred to as the mixed layer model or turbulence closure scheme

---

Differences among models are primarily the choice of numerical methodology to solve for advection and time stepping (including choice of free surface vs. rigid lid) and the subgrid scale parameterizations

- finite differencing scheme - advecto
- " " " - time
- choice of vertical coordinate (z or σ
- type of turbulence closure scheme

Once these above choices are made, we must decide:

- domain and resolution
- boundary conditions

  vertical

    surface forcing (flux or relaxation
    bottom boundary layer (drag)

  horizontal

    mathematical necessity for limited domain model

MAJOR QUESTION:

DO I BUILD MY OWN MODEL OR ADAPT AN EXISTING MODEL?

Two of the more common models today are:

MOM - Modular Ocean Model
derived from Bryan-Cox (GFDL) model

POM - Princeton Ocean Model

$$\frac{\partial F}{\partial t} \approx \frac{F^{n+1} - F^{n-1}}{2\Delta t}$$

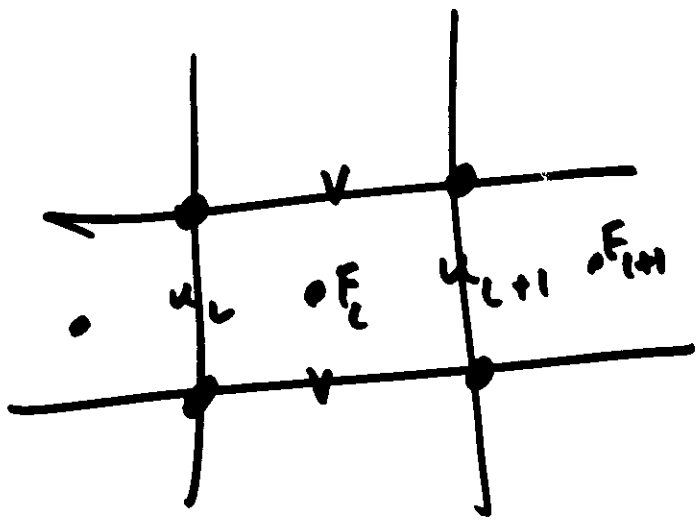

$u \frac{\partial F}{\partial x}$

$$u \frac{\partial F}{\partial x} \approx$$

$$\frac{1}{2}\left[u_i\left[\frac{F_i - F_{i-1}}{\Delta x}\right] + u_{i+1}\left[\frac{F_{i+1} - F_i}{\Delta x}\right]\right]$$

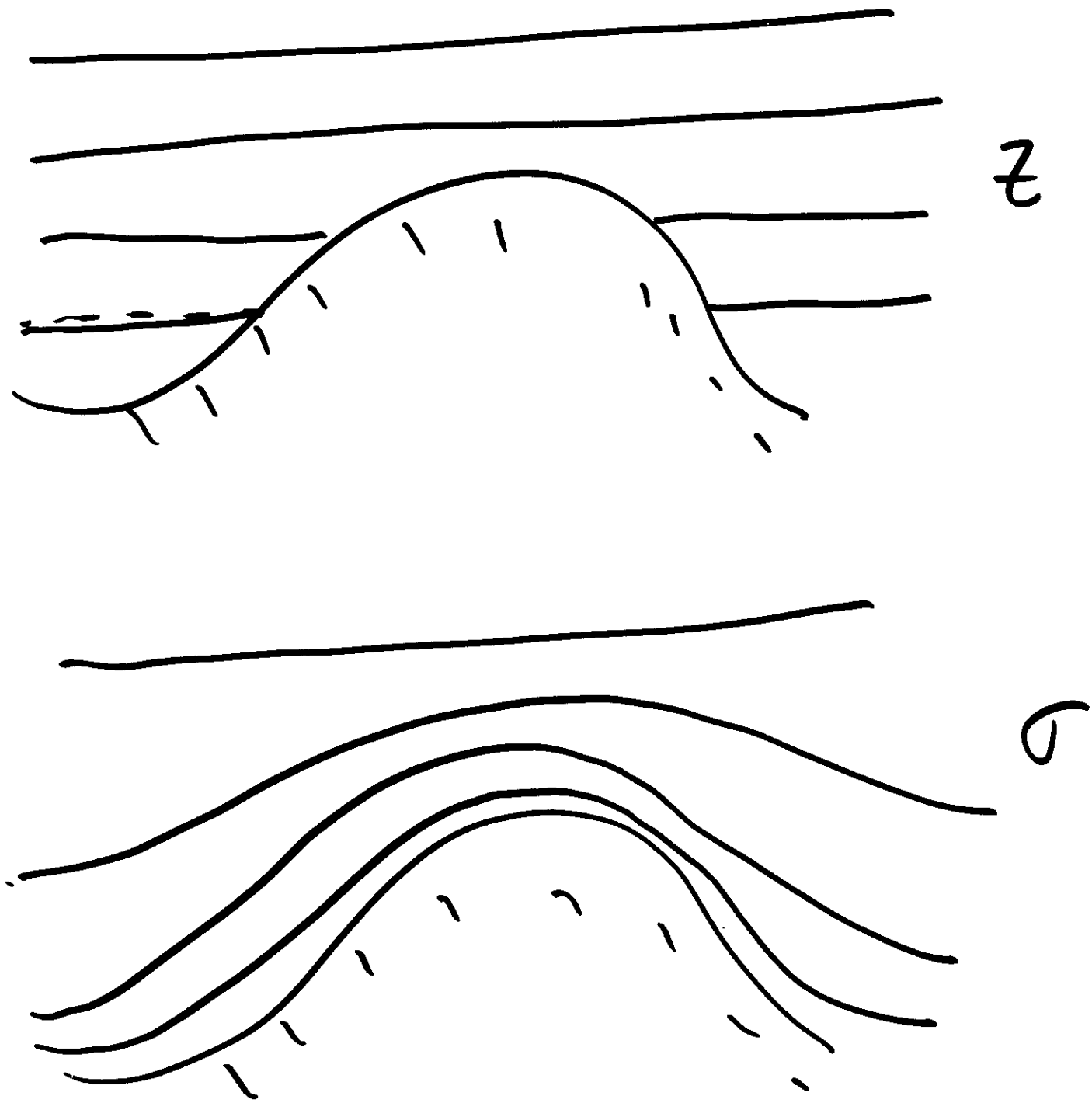
z
σ

Comparison of 5 General CIRC. Models

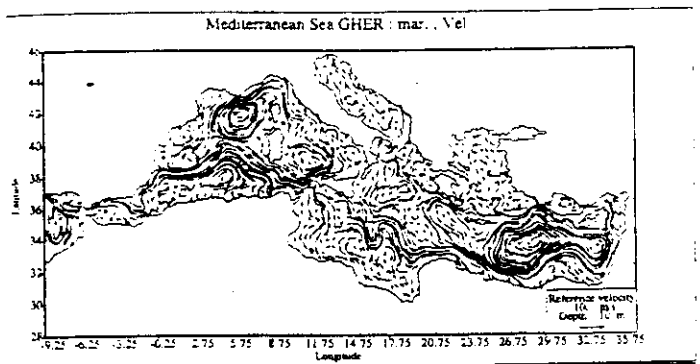

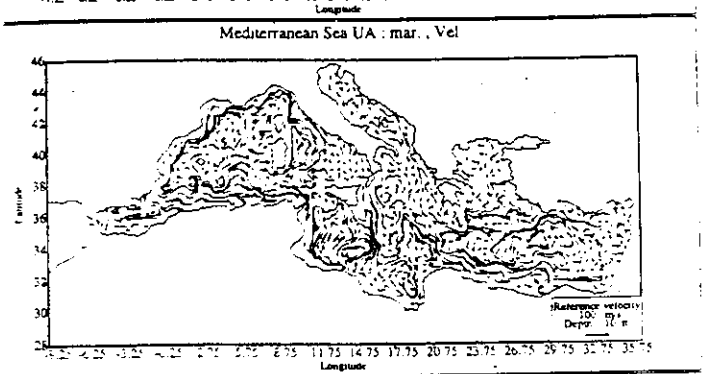

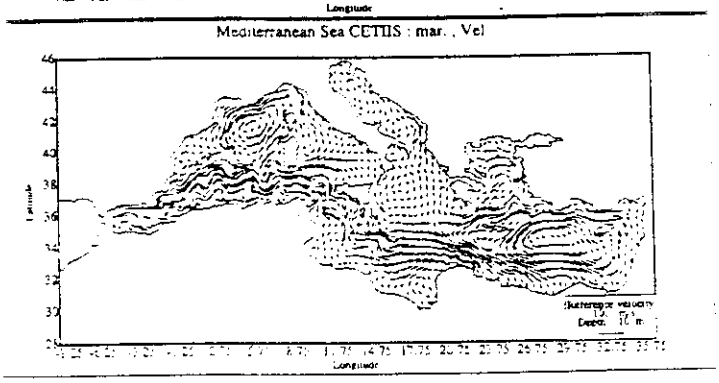

ure 3: Velocity fields March Average

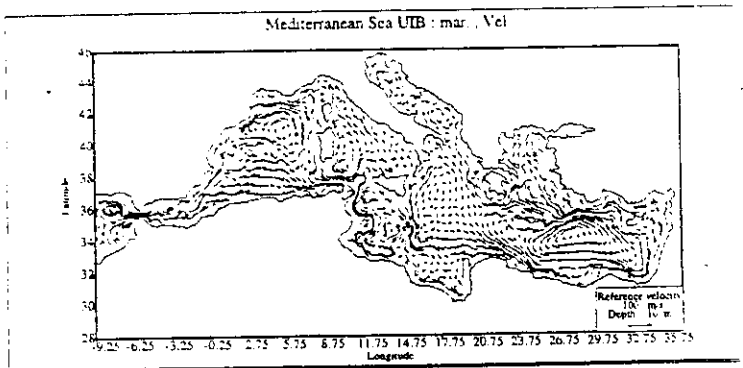

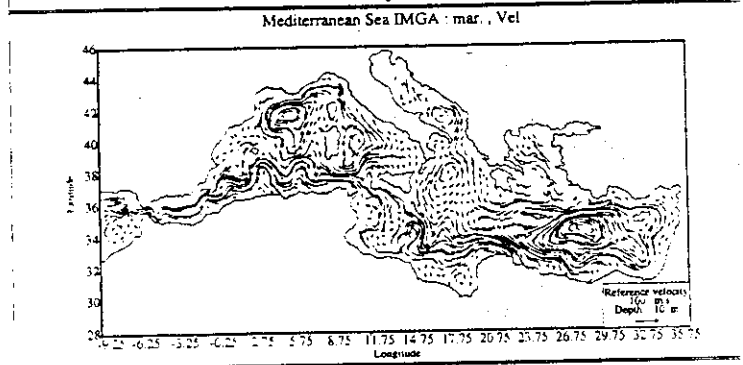

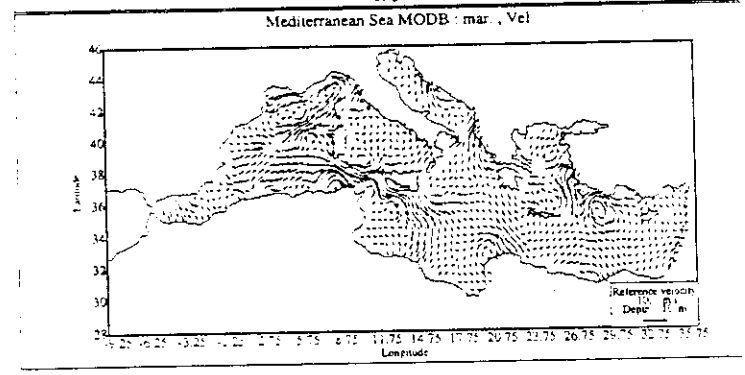

Figure 4: Velocity fields March Average (cont.)

hey differ in the representation of their hydrographic structures. dif-
ent subbasin and small scale feature representation. high frequency
nals in strait fluxes and specific sub-basin drifts ;

Model behaviour depend on modellers skill as much as on models
odel is here understood as the mathematical model and its compu-
implementations, without specified parameters) :

Though the oceanographic relevance of the experiment is not opti-
l (due to the forcing), at least the models exhibit a similar drift, and
know how to correct it ;

Additional calibrations of models (strait adaptations, vertical diffu-
n and modified surface relaxation) could improve "realistic" beha-
our, as shown by some additional simulations of some partners ;

Most of the differences in the hydrographic structures can be explai-
d by the different vertical diffusion parameterisation ;

No model performs clearly better then the others, some give a better
gnal of the variability, some conserve deep water caracteristics bet-
etc. and no real outlyers are visible, except a strong drift in UIB-
OM (and "noisy" UA) ;

Though intercomparison is possible and very helpfull in calibrating
d correcting, a real benchmarking and skill assessment was not pos-
ble, a classical drawback of most intercomparison projects, because
antification of comparison results is only possible on integral quan-
ies, due to the lack of appropriate knowledge of adequate methodo-
gies. For qualitative comparison and improving of models beha-

GHER - U. of Liege (GHER)
UA - U. of Athens (POM)
CETIIS/LODYC - France (OPA)
IMGA - Bologna (MOM)
UIB - U. Illes Baleares (MOM)

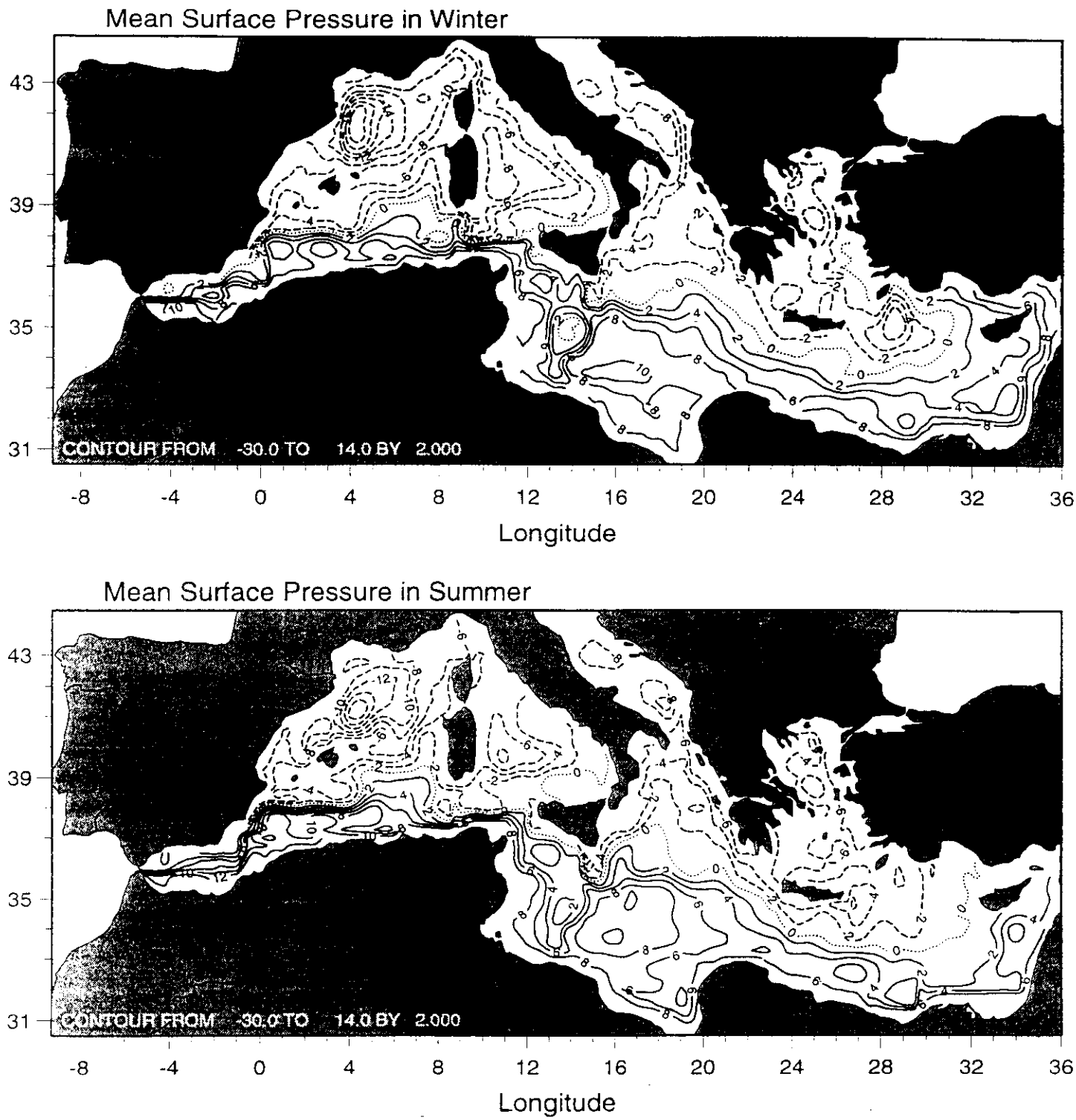

Figure 2. Seasonal mean surface pressure averaged from the last 40 years of the 120-year climatological simulation. Seasons are defined as (top) winter (January, February and March), and (bottom) summer (July, August and September).

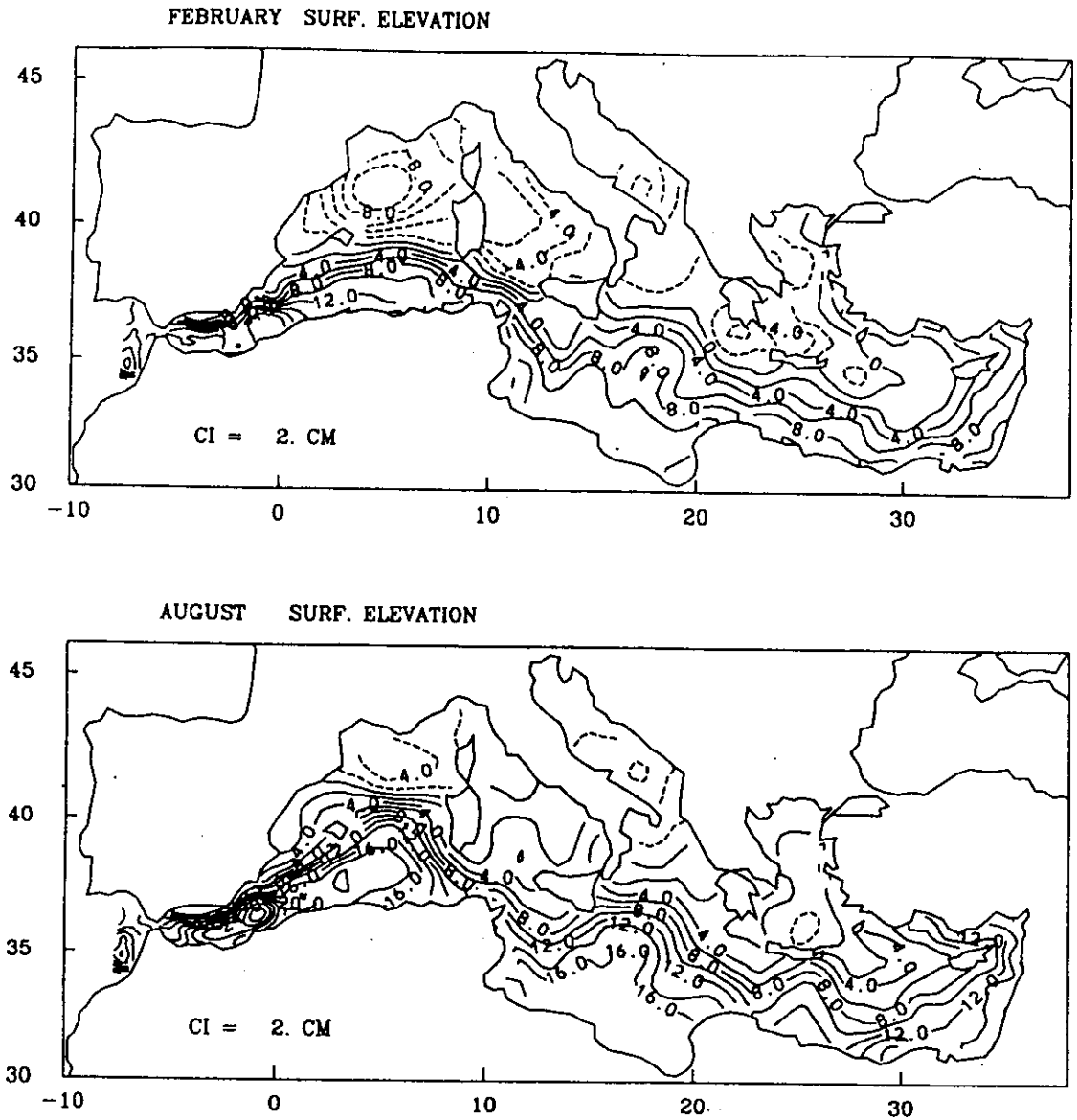

FIG. 14. Surface elevation. (Upper) February; (lower) August. Contour interval is 0.02 m.

FREE SURFACE HEIGHT AND VELOCITY AT 20 M

30 SEPTEMBER YEAR 40

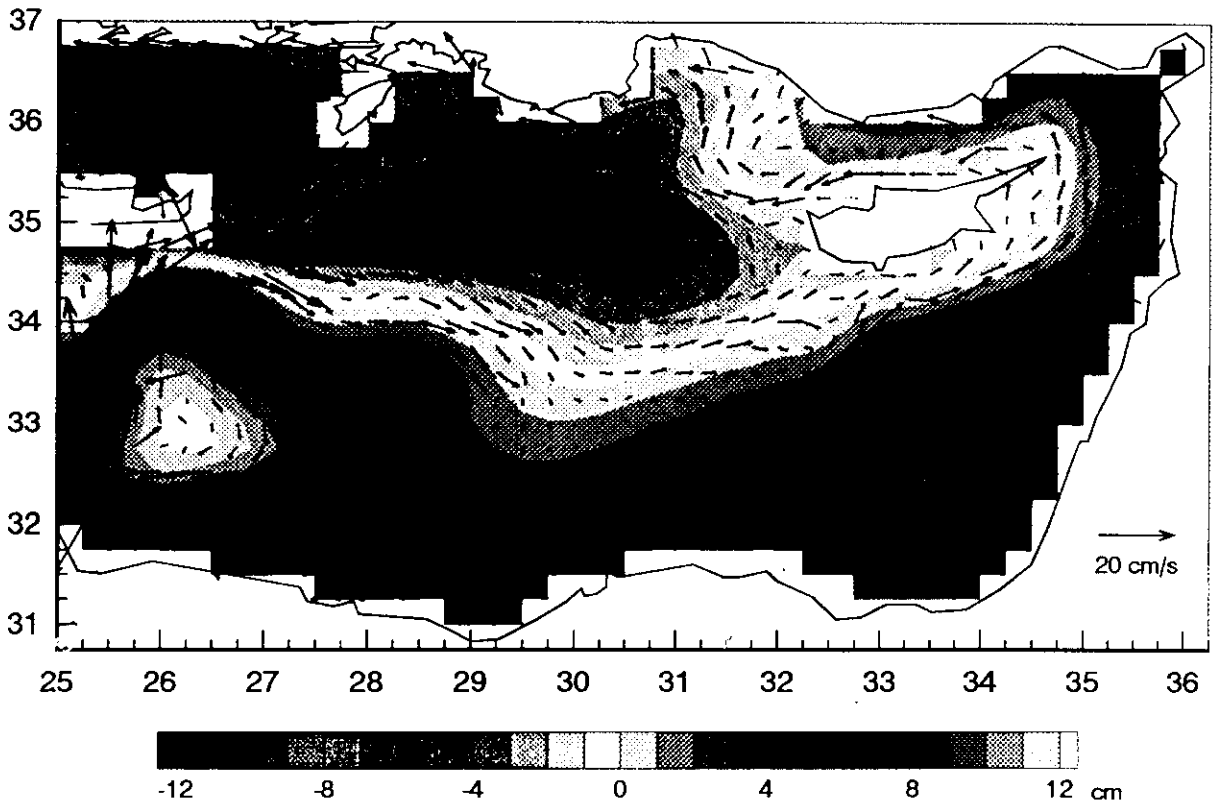

FREE SURFACE HEIGHT AND VELOCITY AT 20 M

1 MARCH YEAR 40

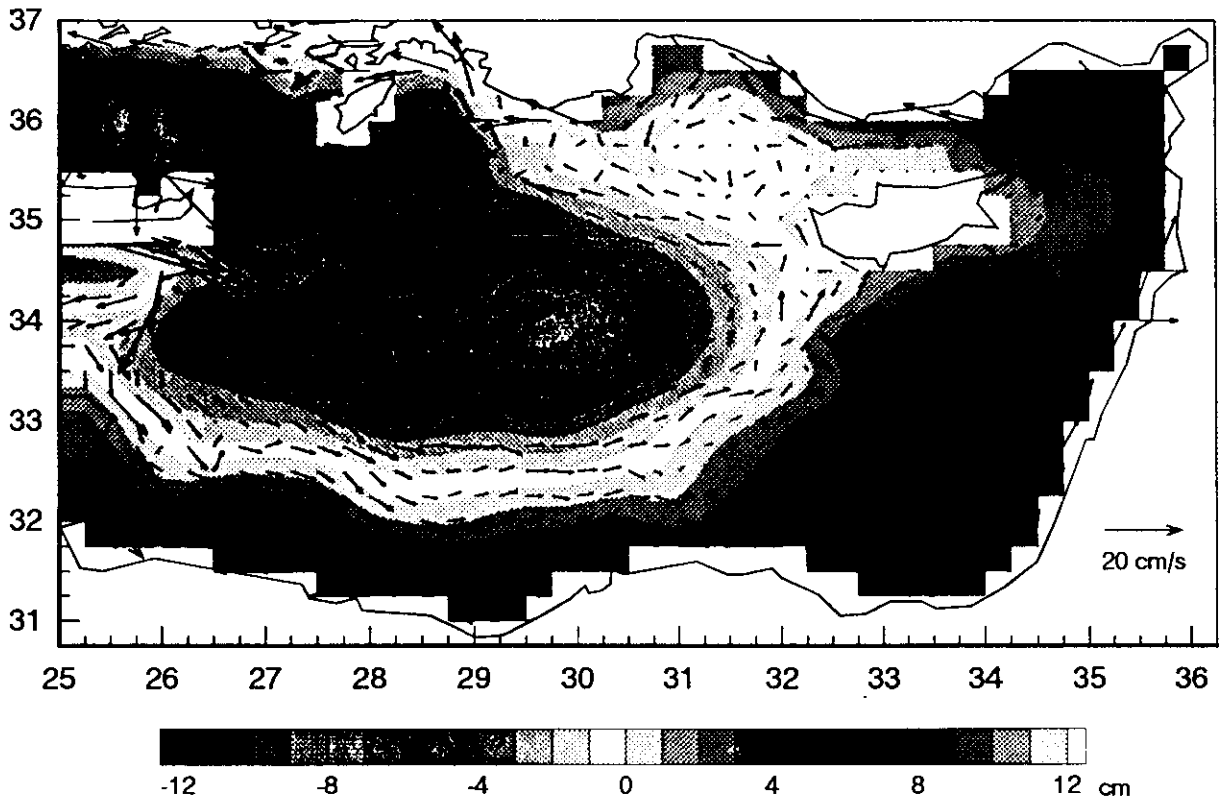

Multiscale interaction

- Redistribution of properties by mesoscale eddies

- Deep water formation
  - Preconditioned region (gyre)
  - Small scale eddies
  - Convective chimney

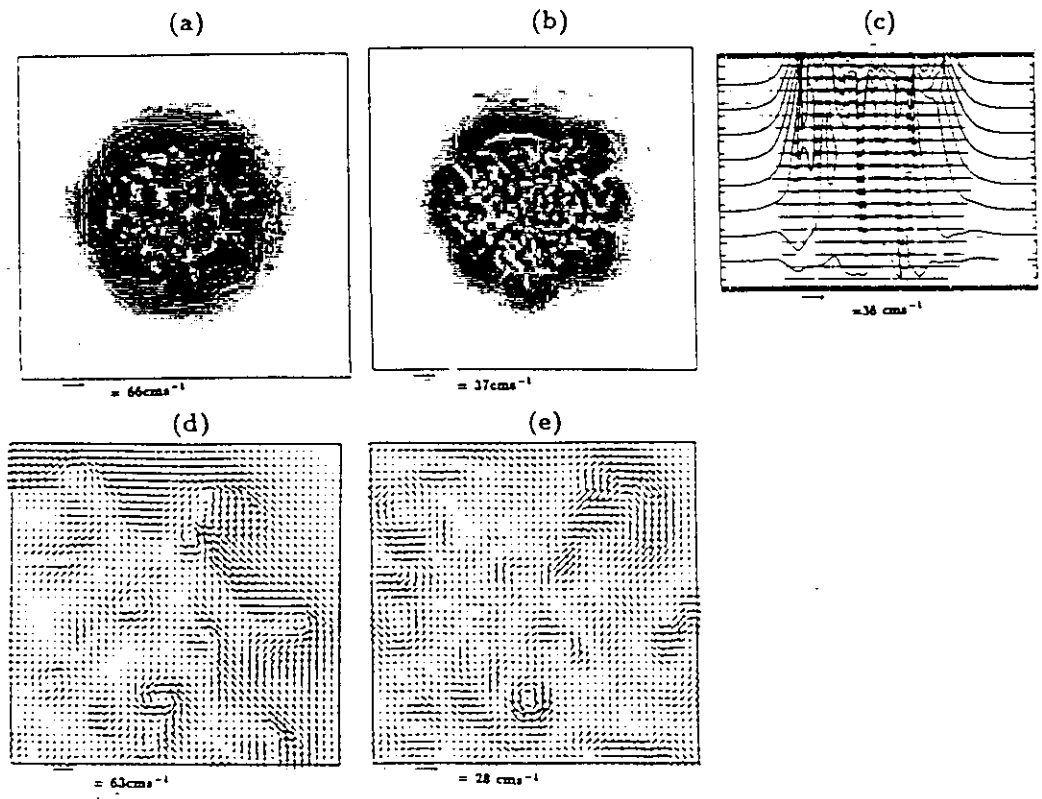

Figure 22: The weakly stratified chimney simulation at day 2, Cooling of 800 Wm^{-2} is applied for 2 day period over a 16 km disk, and then the cooling was turned off to allow the model ocean to geostrophically adjust. a) horizontal currents at 200 m. b) an enlargement of the north-east corner of (a). c) horizontal currents at 1000 m. d) an enlargement of the north-east corner of (b). e) An east-west cross section through the middle of the developing chimneys (Jones and Marshall, 1992).

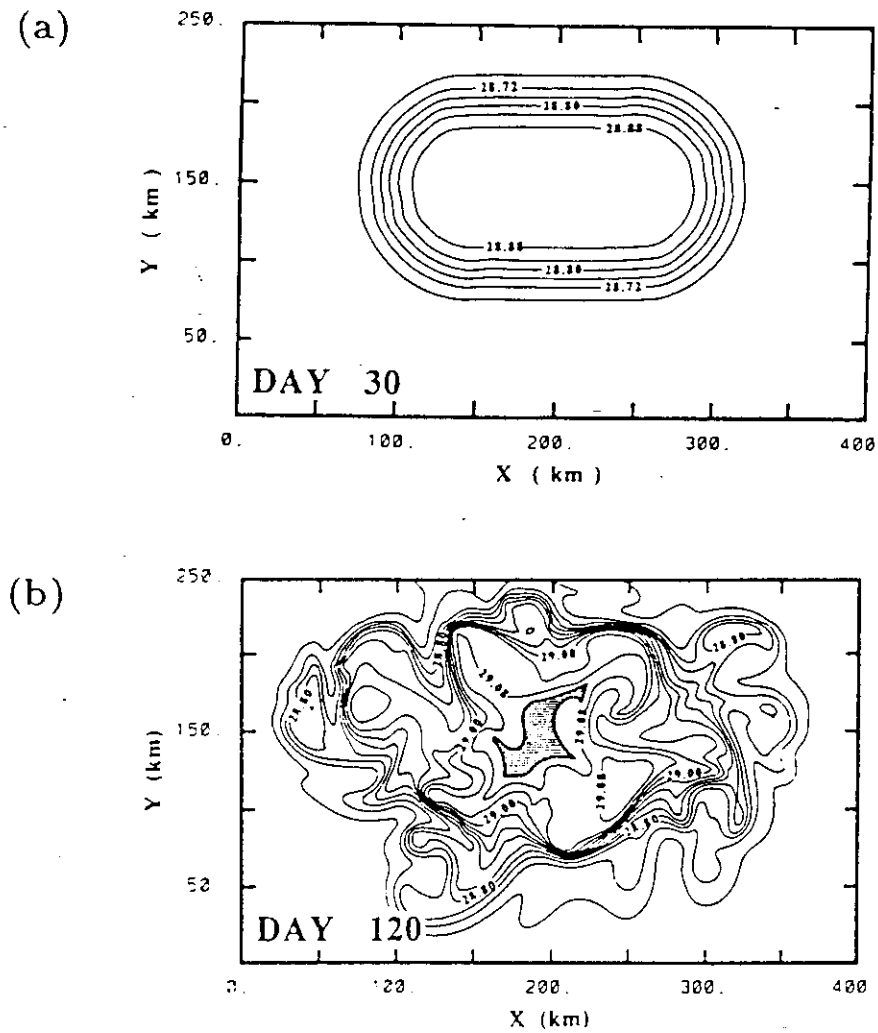

Figure 23: A high resolution 3-D numerical study of deep water formation in the Gulf of Lions with time variability in the thermohalineforcing (Madec *et al.*, 1991). a) day 30, b) day 120.

Gulf of Aqaba (Red Sea)

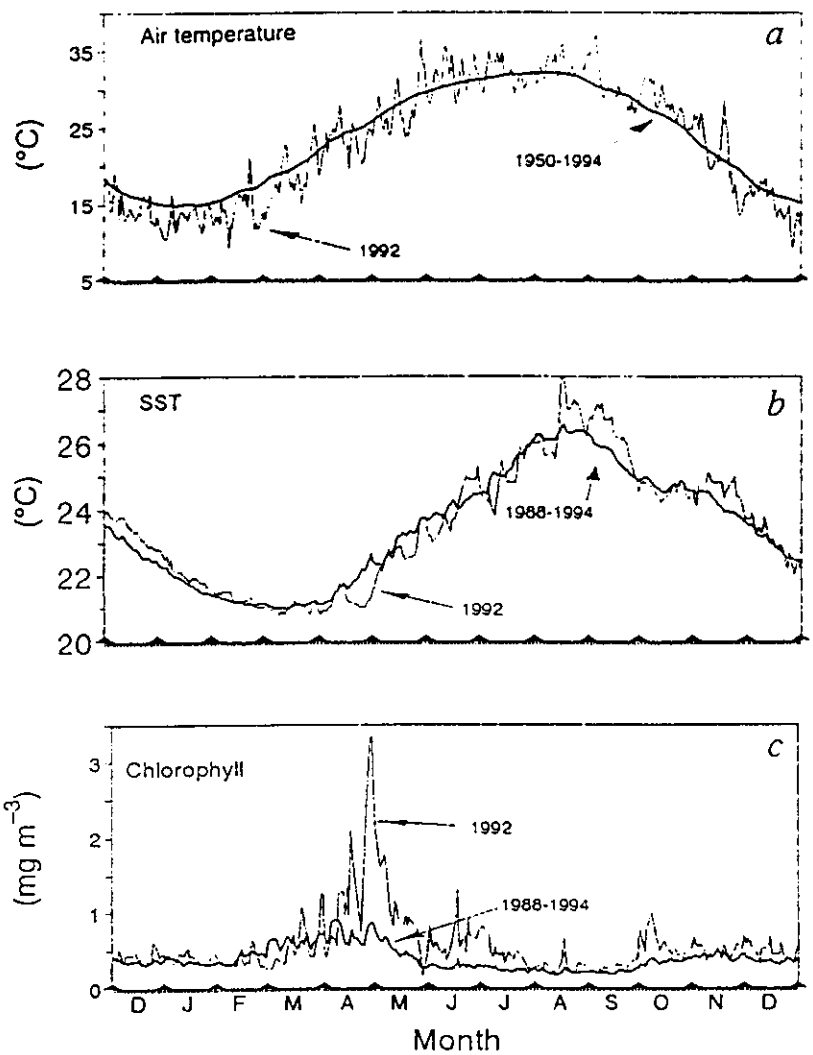

Gulf of Aqaba

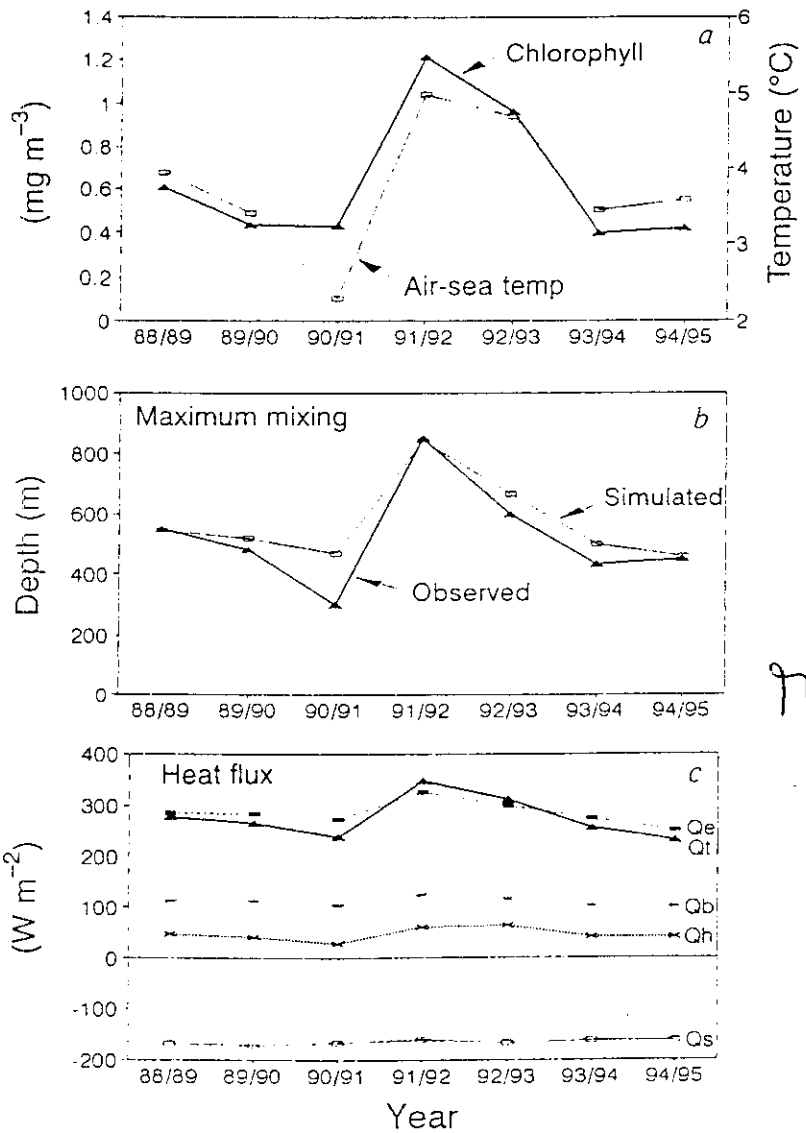

Mellor-Yamada Mixed layer Model

Two way air-sea interaction

- mainly through surface heat fluxes
- important mainly in winter
  - deep and intermediate water formation
  - cyclone tracks
  - influence on precipitation

Mediterranean circulation - Interannual and long term variability

- Response to local and/or remote forcing
- Response to changes in local forcing
- LIW → NADW – Global conveyor belt

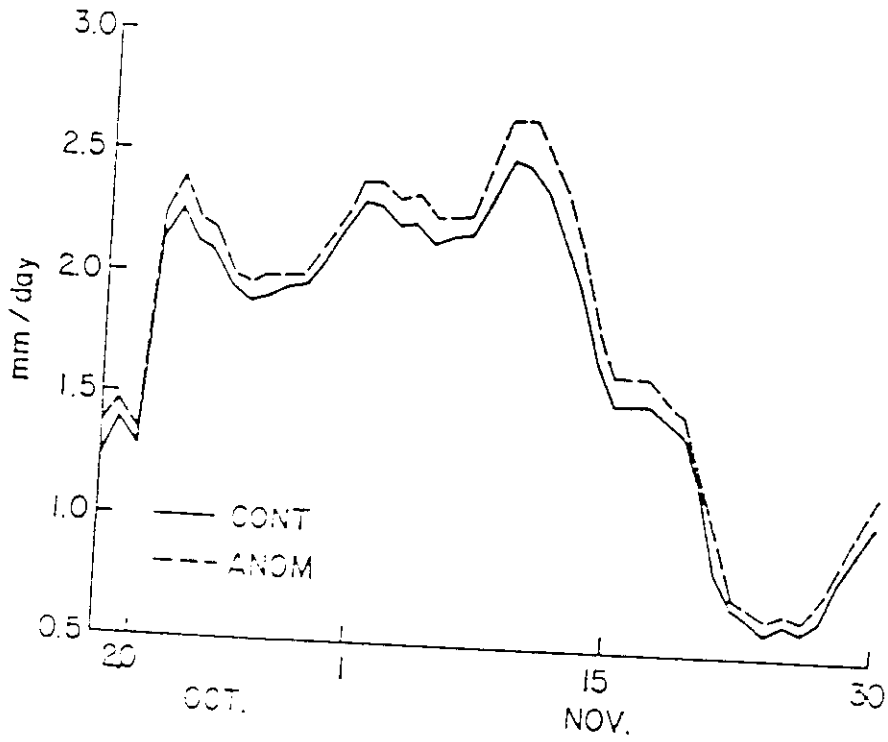

Fig. 1. Twelve-day running mean rainfall in mm day^{-1} over the region 20°–50°N, 20°–45°E. Solid line — control forecasts; dashed line — anomaly forecasts.

In Fig. 2 we show the total rainfall in mm day^{-1} for the entire 44 days of the 11 control forecasts. There are three regions where the precipitation field exhibits relative maxima. The most intense is located in the northwest corner of the map off the Atlantic coast of France. This is associated with North Atlantic storms which cross central and northern Europe. In general, these storms do not affect the eastern Mediterranean region. The second maximum appears as a tongue of precipitation greater than 3 mm day^{-1} over the Adriatic Sea and Yugoslavia. The third maximum occurs over the eastern end of the Mediterranean (values greater than 2 mm day^{-1}) and extends eastward into Iraq (off the edge of the map). For comparison, Fig. 3 shows the climatological precipitation for the months of October, November, and December from Jaeger (1976). From these two figures it can be seen that the model-produced precipitation is quite reasonable in both amount and location. Much of the difference between the model and climatology can be attributed to interannual variability. This result is quite encouraging considering the coarse resolution of the model.

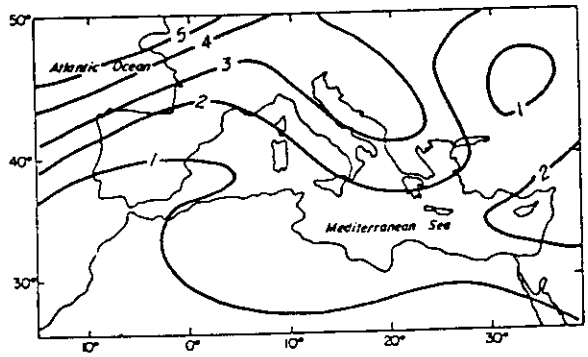

Fig. 2. Total rainfall in mm day^{-1} for the entire 44-day period of the 11 control forecasts. The contour interval is 1 mm day^{-1}.

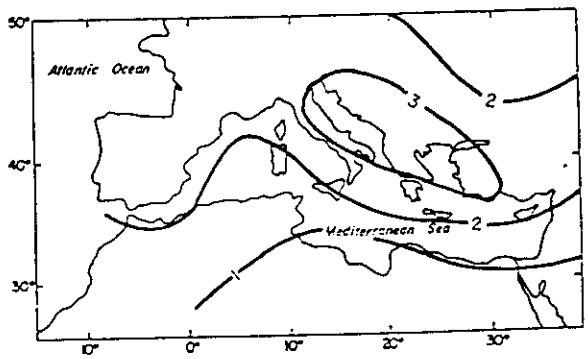

Fig. 3. Climatological rainfall in mm day^{-1} for the months of October, November, and December (from Jaeger, 1976). The contour interval is 1 mm day^{-1}.

The changes in the precipitation field for the entire 44-day period are shown in Fig. 4 where we have plotted the values of ANOM – CONT. The shading indicates statistical significance at or above the 5% level based on a *t*-test for paired comparisons. The significant increase in precipitation is confined mainly to the Levantine Sea and the surrounding area. Maximum increases of 0.6 mm day^{-1} or more appear as a band which follows the coast of Turkey. Over central and northern Israel and Lebanon, the increase of 0.4 mm day^{-1} corresponds to 15–20% of the total rainfall for that area. There is a slight decrease in the rainfall across eastern Europe, over Algeria, and over parts of Spain and France. However these decreases are not statistically significant.

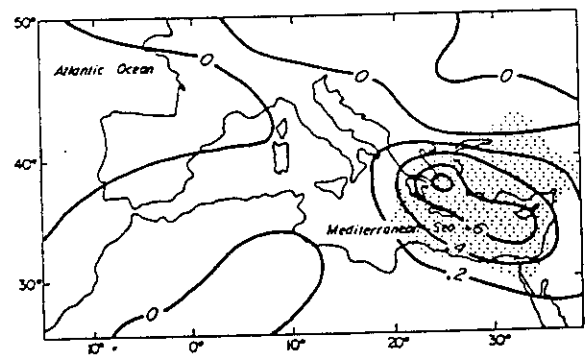

Fig. 4. ANOM – CONT rainfall difference for the same period as in Fig. 2. Shading indicates the 5% statistical significance level. The contour interval is 0.2 mm day^{-1}.

In order to further understand the physical processes responsible for this increase in precipitation we compared the mean circulation for the control and anomaly runs in the lowest model layer. We found that the wind components and the height field did not differ substantially (e.g., ANOM – CONT differences in the wind components were at most a few tenths of a meter per second). However, the temperature of the lowest model layer did show significant changes, as indicated in Fig. 5. Over the area of the imposed sea surface temperature anomaly, the mean temperature for the 11 anomaly forecasts was at least 0.5 °K warmer than in the corresponding control cases. This is due to the change in the sensible heat flux from the warmer sea in the anomaly runs. The maximum sensible heat flux to the south of Cyprus increased from 44 W m^{-2} for the control runs to 67 W m^{-2} in the anomaly runs. The lapse rate from 1000 to 850 mb increased from 7 °K/km in the control runs to 7.5 °K/km in the anomaly runs.

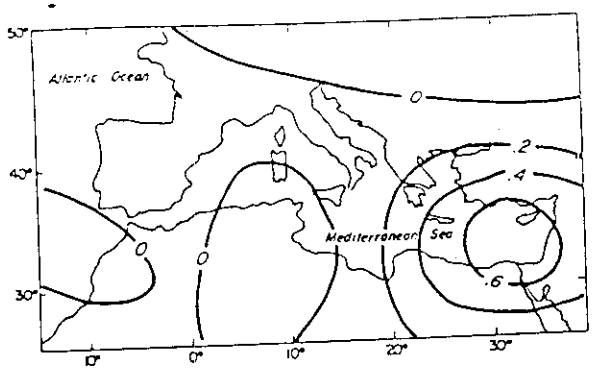

Fig. 5. ANOM – CONT difference in the temperature of the lowest model layer for the entire 44-day period. The contour interval is 0.2 °K.

The resulting decrease in the static stability led us to suspect that the convective activity increased in the anomaly runs. We were able to check this easily since the model computes the large-scale and convective rainfall separately. Fig. 6 shows the convective components of the total control rainfall. Recalling the three precipitation maxima that appeared in Fig. 2, we can now see that the maximum in the northwest corner of the map is due mainly to large-scale precipitation. The land-based part of the high rainfall tongue that appeared over Yugoslavia is mainly due to the large-scale condensation, while the part of this tongue over the Adriatic Sea is due to convective activity. It appears that the

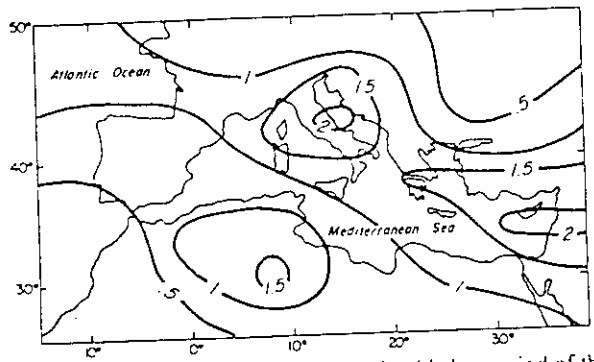

Fig. 6. Convective rainfall for the entire 44-day period of the eleven control runs. The contour interval is 0.5 mm day^{-1}.

former is related to orographic lifting while the latter is related to convective activity over the relatively warm sea. The third maximum which extended from the Levantine Sea across Israel, Lebanon, Syria, and into Iraq is due almost exclusively to convective rainfall. The convective rainfall occurs in a band that is oriented along the major axis of the eastern Mediterranean. Apparently the convective activity is triggered by the temperature contrast between the relatively warm sea and the cold land surfaces to the north. We also note that of the increase in total rainfall in the anomaly runs (over the shaded area in Fig. 4), roughly 80% of the change is due to the increase in convective precipitation and 20% is due to the increase in the large-scale condensation.

In order to determine the primary cause of the increase in rainfall (i.e., enhanced evaporation or destabilization), three additional experiments were run from each of the 11 sets of initial conditions. The results of these experiments are summarized in Table 1. For comparison we have also included the control (first line of Table 1) and anomaly (last line) results. Each of these experiments isolated a different aspect of the anomalous surface fluxes as follows: ANSH — the SST anomaly was allowed to affect the sensible heat flux only (i.e., no enhanced evaporation); ANLH — the SST anomaly was allowed to affect the latent heat flux only; and LAND — all eastern Mediterranean grid points were treated as land so that evaporation was effectively cut off. From the table we can see that over the region of significant change, the rainfall in the anomaly runs increased by 0.22 mm day^{-1} or by 17%. Two-thirds of this increase was due to the destabilization of the lower atmosphere by the anomalous sensible heat flux, as

Table 1. Average rainfall over the region 29°–40°N, 20°–38°E

Experiment*	Rainfall (mm day^{-1})	Increase** (mm day^{-1})	Increase** (%)
CONT	1.28	---	---
ANSH	1.43	+0.15	+12
ANLH	1.32	+0.04	+ 3
LAND	1.10	–0.18	–14
ANOM	1.50	+0.22	+17

* See text for explanation of experiments.
** Increase relative to the control (CONT) experiment.

indicated by the ANSH results. The additional moisture introduced by the enhanced evaporation (ANLH) accounted for only a small part of the total increase. The sum of the ANSH and ANLH increases was less than the total anomaly increase due to the nonlinearity of the processes involved. Finally, removing the eastern Mediterranean as a moisture source (LAND experiments) led to a reduction in the rainfall of 0.18 mm day^{-1} or only 14%.

CONCLUSION

Results have been presented from a series of numerical experiments designed to study the influence of the eastern Mediterranean Sea on the precipitation of the

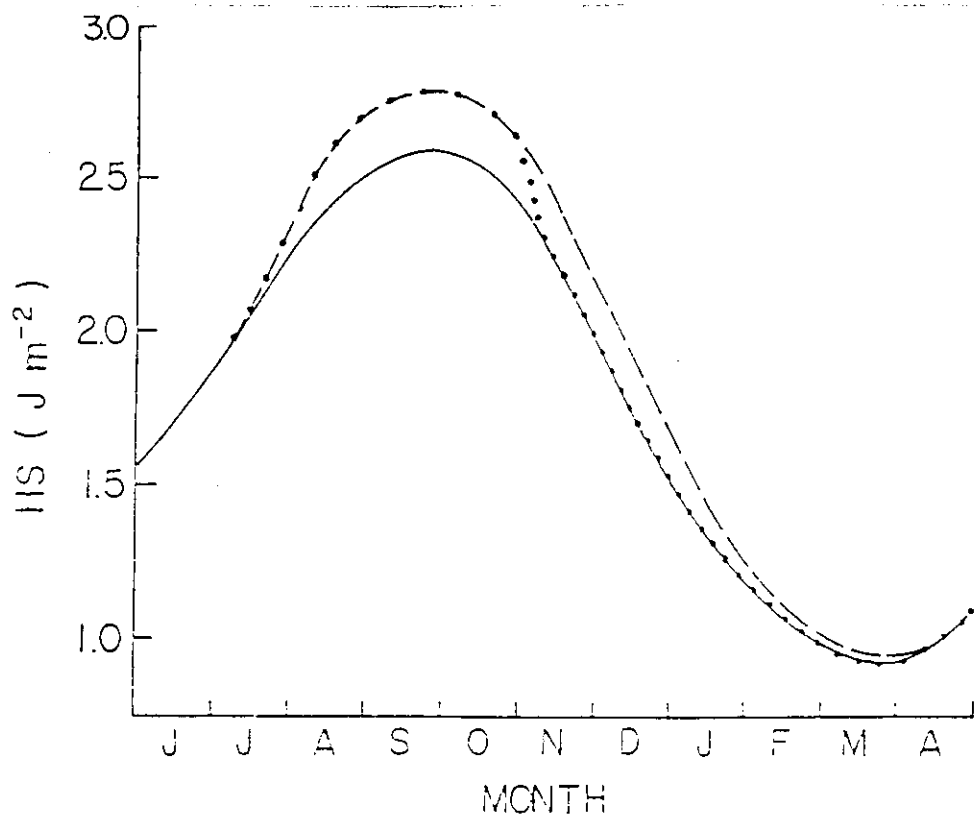

Fig. 2. Heat storage cycle in the layer 0-150 m for: control run (solid line), enhanced summer mixing (dashed line), and enhanced summer mixing plus storm on 1-4 November (dotted line)

b. Boundary conditions

heat fluxes. Thus we devised the following simple

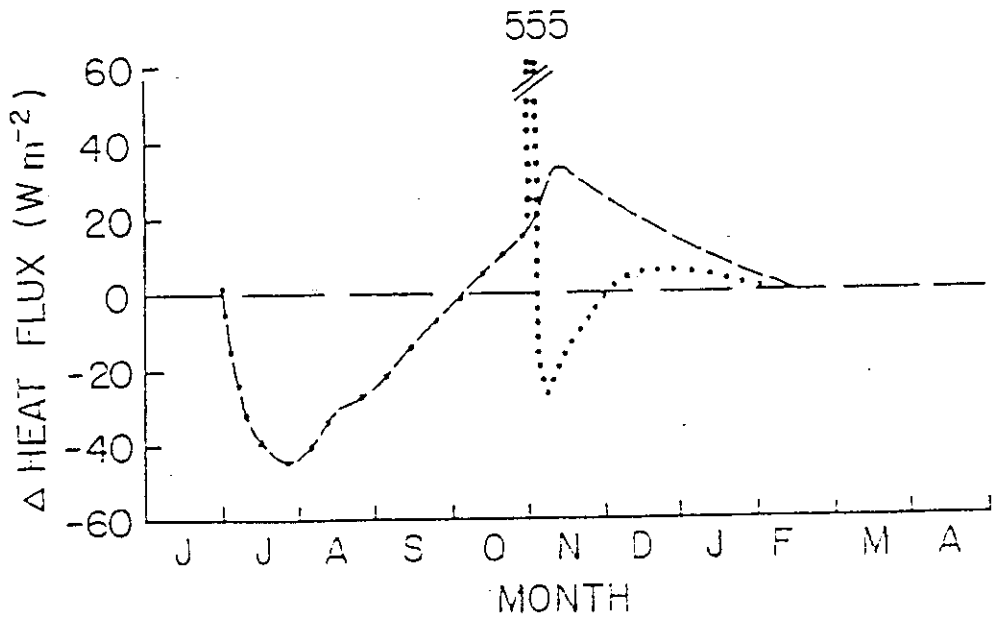

Fig.3. Difference between predicted and climatological turbulent heat flux (latent + sensible) for: the enhanced summer mixing case (dashed line) and the enhanced summer mixing with a storm on 1-4 November (dotted line).

1-D Bulk (Kraus-Turner) mixed layer model